Critical Scaling of Novelty in the Cortex

Tiago L. Ribeiro, Ali Vakili, Bridgette Gifford, Raiyyan Siddiqui, Vincent Sinfuego, Sinisa Pajevic, and Dietmar Plenz†

Section on Critical Brain Dynamics, National Institute of Mental Health, Bethesda, MD, USA

† Correspondence: plenzd@mail.nih.gov

Running Title: Critical scaling of novel cortical action potentials *in vivo*

Correspondence: Dietmar Plenz, Ph.D., Section on Critical Brain Dynamics, National Institute of Mental Health, Porter Neuroscience Research Center, Rm 3A-1000, 35 Convent Drive, Bethesda, MD 20892. office: (301) 675-5311

Keywords: Perturbation, population coding, criticality, scaling, neuronal avalanches, visual cortex, *in vivo*, 2-photon imaging, holography, all-optical

Abstract

The ability to detect unanticipated, novel events and rapidly relay this information across neural networks is fundamental to brain function, enabling the selection of appropriate behavioral responses. Here, we examine the transmission of holographically triggered action potentials in primary visual cortex of quietly resting mice, focusing on the dynamics of communication from pyramidal neurons. We demonstrate that these novel action potentials, which are uncorrelated with preceding activity, exert a disproportionally large influence on neighboring neurons. Their influence scales robustly to an exponent between 0.2 and 0.3 relative to their number. Remarkably, even a small number of novel action potentials can engage a majority of the local network, achieving high decoding accuracy of the perturbation origin in the face of high trial-by-trial variability and ongoing activity characterized by scale-invariant, parabolic neuronal avalanches. This heightened susceptibility to small, local perturbations aligns with the behavior of complex systems exhibiting critical dynamics. Our findings reveal that scaling underpins the efficient communication of unanticipated action potentials, suggesting it is a fundamental mechanism for detecting and processing novel events in the brain. These results provide new insights into the neural basis of novelty detection and highlight the importance of critical dynamics in cortical network function.

Introduction

Thriving in uncertainty requires detecting and responding to the unexpected. In mammals, unexpected events must be effectively communicated within and across brain areas to ensure accurate evaluation and appropriate behavioral responses[1]. A key step in this process is how novel action potentials in the cortex – those in a single pyramidal neuron that exceed near-future expectation based on ongoing activity – are transmitted to the surrounding cortical network.

Neuronal spiking has been found to shape cortical activity and behavior. A spike in a pyramidal neuron from superficial layers (L2/3) of cortex of mice has been estimated to influence fewer than 1% of nearby neurons, to evoke strong local inhibition[2-5], and in reptilian cortex to reliably recruit activity sequences[6]. Coordinated activity in small groups of L2/3 pyramidal neurons elicits spatially extended variable responses[7] and can drive trained behavior via pattern completion[8,9]. Similarly, spike bursts in deep layers (L5/6) can elicit sensitized behavioral responses[10,11] and alter global brain states[12,13]. These optogenetical studies in mice are in line with previous findings from cortical microstimulation in primates highlighting the capacity of few spikes to significantly alter brain activity under specific conditions (for review[14]). However, a comprehensive framework to quantify the impact of action potentials on the spatiotemporal dynamics of cortical networks remains elusive.

In principle, novel spikes representing unexpected events should induce propagation across the cortex both broadly (to reach multiple functional domains for evaluation given their uncertain nature) and rapidly (to be able to act quickly). However, this dissemination of information is constrained by several factors. First, even in the resting state, the cortex exhibits substantial activity, with individual neurons receiving thousands of action potentials every second. Accordingly, individual neurons operate in a fluctuation-dominated[15], high-dimensional[16] regime that shapes their ability to respond to and encode information from novel spikes[17] or sensory inputs[18]. Second, the sparse synaptic connectivity between L2/3 pyramidal neurons — estimated at only 5–8% and diminishing sharply within 200 μm[19-23] — further restricts the transmission of novel spikes[24]. Additionally, the weak and transient synaptic currents of these failure-prone connections in vivo[2,22], coupled with strong local inhibition[25,26], further reduce the potential influence of novel spikes introduced randomly into a pyramidal neuron in the awake state. Given these limitations, understanding how novel spikes are encoded requires a focus on the network's broader dynamics rather than the activity of individual neurons or microcircuits. However, adopting this broader perspective presents a significant challenge due to the inherent complexity of cortical activity.

Research suggests that brain networks operating near a critical state exhibit heightened sensitivity to small perturbations[27,28], which might enable the cortex to detect and process new information despite its complex internal activity and sparse topology. In this state, the system undergoes internal fluctuations while remaining responsive to small, local events that can propagate broadly, facilitating the recognition and dissemination of novel information. In the superficial cortical layers, these fluctuations manifest as "neuronal avalanches" — scale-invariant patterns of synchronized neuron activity characteristic of the awake state[29-31]. These avalanches align with theoretical predictions of critical dynamics. However, direct experimental evidence demonstrating that novel, localized information propagates within the neuronal avalanche regime and scales in line with predictions from critically is lacking, leaving a gap in understanding whether and how criticality supports the spread of novel information in the brain.

Using an all-optical approach, we holographically triggered spikes in individual L2/3 pyramidal neurons in the primary visual cortex of awake mice during spontaneous, ongoing avalanche activity. Simultaneously, we recorded the activity of hundreds of nearby neurons. Our results demonstrate robust scaling of network responses, with novel spikes rapidly generating widespread, information-rich activity across large cortical distances. These findings align with predictions for responses to small perturbations in critical systems, highlighting the role of critical dynamics in efficient cortical information processing.

84 ## Results

85 **Holographically triggered spikes in a pyramidal neuron induce rapid, widespread excitation in**
86 **superficial cortical layers**

87 In awake, quietly resting adult mice, we holographically targeted single L2/3 pyramidal neurons (Target
88 Cells, TC) in primary visual cortex (V1) that were chronically co-expressing the calcium indicator
89 jGCaMP7s and the opsin ChrimsonR (5 to 10 mW, 100 ms; ~100 – 150 trials per TC) while
90 simultaneously monitoring spiking activity from more than hundred nearby neurons using 2-photon
91 imaging (field of view: 450 µm x 450 µm; 50 – 140 µm cortical depth; temporal resolution: 22 ms; n = 6
92 mice; 16 experiments). Sparse co-expression, stimulation beam profiling, and anatomical
93 reconstruction confirmed select single neuron stimulation (Fig. 1a; Supplementary Figs. 1–3).
94 Holographic stimulation of a single pyramidal neuron caused rapid and wide-spread effects
95 across the surrounding network. Within 132 ms, approximately 15% of non-targeted neurons increased
96 spiking (Positive Responders, PosR), while fewer than 1% showed decreased spiking (Negative
97 Responders, NegR), despite high trial-to-trial variability (Fig. 1b, c; 2.5% significance threshold, one-
98 tailed Welch's *t*-test). Baseline activity was consistent across all groups (TC, PosR, NegR, and non-
99 responders, NonR), with neurons exhibiting spike count variability well above Poisson expectations
100 (Fig. 1d; baseline; n = 54 TC; n = ~9,000 PosR, NegR, NonR). Upon stimulation, PosR firing rates and
101 spike count variance increased markedly remaining well above expectations for a Poisson process as
102 reported previously[32] (Fig. 1d; response).
103

104 **Novel spikes scale network responses without change in overall network variability**

105 Holographically triggered spikes in TC neurons were classified as "novel" because they were not
106 predicted by ongoing activity, as demonstrated by autocorrelation analysis. During the baseline period,
107 ongoing spiking exhibited significant temporal order, with high autocorrelation across all groups ($r \approx 0.2$,
108 Fig. 2a, b; base' vs. base). However, during the response, the autocorrelation for TC neurons (base vs.
109 resp) dropped to nearly zero ($r \approx 0$; $p < 10^{-3}$, Wilcoxon rank sum), indicating that stimulation introduced
110 spikes randomly, disrupting the temporal organization of ongoing TC spiking. In contrast, temporal
111 correlations remained stable for PosR and NonR, while the observed decrease in NegR autocorrelation
112 reflected overall reduction in sparse spiking (Fig. 2b).
113

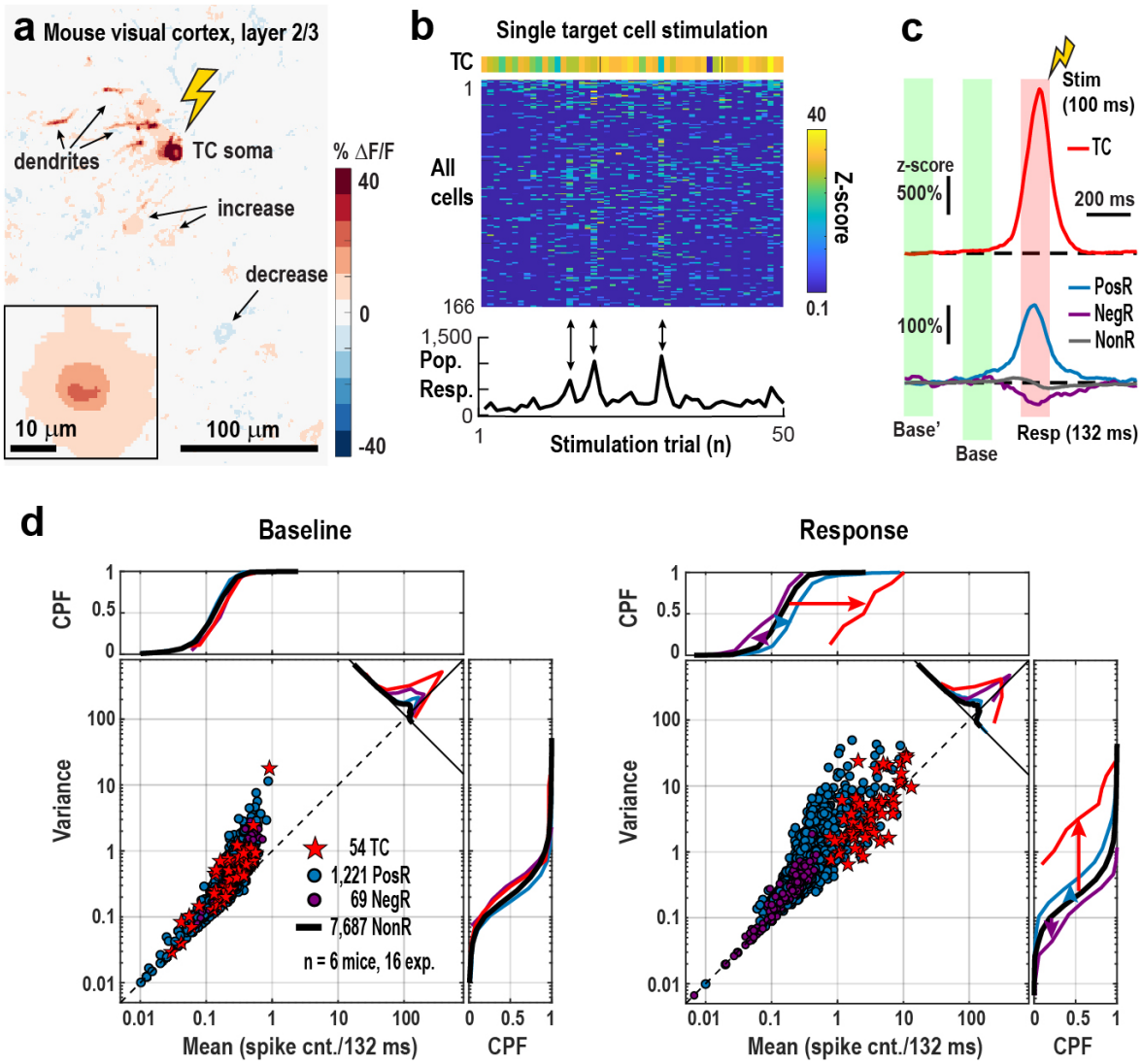

Fig. 1 | Holographically triggered spikes in a single pyramidal neuron rapidly elicit significant excitation in many visual cortex neurons during ongoing activity at rest. a Holographic stimulation (100 ms, *flash;*) targeting a single pyramidal neuron (*TC*; averaged over n = 150 trials) alters the relative fluorescence in the TC *soma*, its *dendrites*, and neighboring neurons (indicated by *arrows*), reflecting changes in spontaneous spiking activity. *Inset*: Mean from n = 54 TC somata. **b** Example of variable spike count (z-scored) in a holographically targeted TC (100 ms, 5mW stimulation) and neurons within a 450×450 µm² field of view (n = 166, ranked by mean spike count within 132 ms of stimulation; n = 50 consecutive trials; single experiment). *Bottom*: Summed z-score of population activity per trial, highlighting overall network response. *Arrows* indicate trials with a high number of co-active neurons. **c** Mean transient response to short-lasting holographic stimulation. Average time course (n = 6 mice; 16 experiments) of z-scored spike count at frame rate resolution (22 ms) for n = 54 TC, n = 1,221 Positive Responders (*PosR*), n = 69 Negative Responders (*NegR*) and n = 7,687 Non-significant Responders (*NonR*). Protracted and prolonged reconstructed responses are observed due to deep interpolation (see Supplementary Fig. 7). *Base', Base* and *Resp* indicate respective time windows of analysis. *Yellow bar*: Stimulation window. **d** The response to single TC stimulation is largely excitatory, while maintaining variability above Poisson-level expectation (*dashed line*). Summary scatterplot of variance vs. mean spike count/132 ms for baseline and response (n = 6 mice, n = 16 experiments). Approximately 15% of neurons exhibit a significant increase in spike count from baseline (*PosR*), while fewer than 1% show a significant decrease (*NegR*). For *NonR*, only marginal distributions are shown. *CPF*: Cumulative Probability Function.

Spike count changes in TC in relation to other neuron categories exhibited distinct differences for baseline and response which we quantified using cross-correlations and scaling functions. During baseline, TC spike counts (TC_{sc}) were significantly correlated with all groups (<cc> ≈ 0.05; Fig. 2c) and followed a consistent scaling relationship:

$$PosR_{sc},\ NegR_{sc},\ NonR_{sc} \sim TC_{sc}^{h}, \quad (1)$$

with h ≅ 0.5 (linear regression; Fig. 2d). This scaling applied both to per-neuron spike counts and totals across all neurons and was observed for the majority of baseline fluctuations from 1 to ~ 7 spikes/132 ms (transient firing rate increases of 8 – 53 Hz; see also Supplementary Fig. 4).

Upon stimulation, the excitatory response in PosR showed similar scaling:

$$PosR_{sc} \sim TC_{sc}^{h}, \quad (2)$$

with a significantly lower exponent of h ≅ 0.3 (linear regression; Fig. 2e, f). In contrast, NonR exhibited no scaling, while NegR showed negative scaling. This demonstrates that network responses to single spikes scale similar to responses to multiple novel spikes from a single neuron. Despite our partial control of holographical spike generation due to variability from external (e.g., head movement) and internal (e.g., network inhibition) factors, these scaling relationships, nevertheless, derived a posteriori by averaging trials, confirm that driving a single pyramidal neuron distinctly affects neuronal populations compared to baseline. Our 1–7 added spikes per 132 ms closely match the 1–7 spikes/132 ms seen in spontaneous fluctuations, showing our holographic manipulation stays within normal cortical firing ranges (<20% of trials exceeded 7 spikes/132 ms).

The distinct scaling relationships between TC stimulation and the excitatory network response was mirrored in corresponding positive, zero, and negative cross-correlations between TC and the other neuron categories (Fig. 2c). The positive cross-correlation found for TC and PosR exhibited only weak overlap in evoked and functional connectivity (R^2 = 0.018; linear regression), demonstrating that novel spikes scale with neighboring sub-networks largely unexplored during ongoing activity. These scaling relationships were robust to the significance level alpha employed. At ~10 times lower alpha, the scaling exponent *h* for PosR was still close to 0.2 (Fig. 2g).

The sparse synaptic connections between local L2/3 pyramidal neurons — estimated at only 5–8% and largely absent beyond 200 μm[19-23,33] suggest that among 200 neurons observed, less than 16 neurons are synaptically connected to a given TC. PosR were consistently found near TCs within a ~200 μm radius as reported previously[4], in line with expectations for locally connected neighbors providing the strongest spike count increases. However, a substantial portion of PosR was distributed throughout the network (Fig. 2g–h) and this proportion increased as the significance threshold (α) was lowered. At the lowest significance level examined, nearly half of all recorded neurons showed significant positive responses, with an average scaling exponent of $h \geq 0.25$.

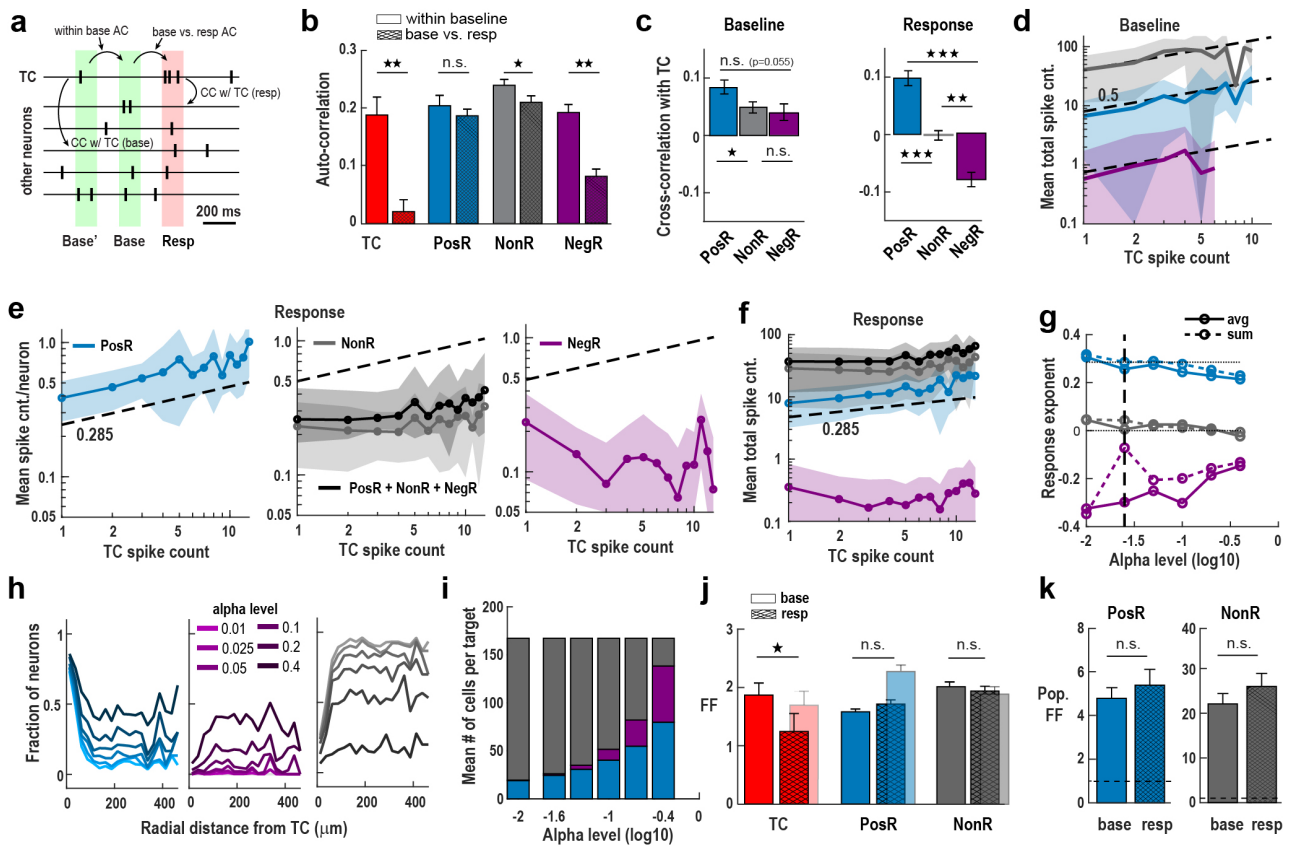

Fig. 2 | Scaling of cortical network responses to novel, holographically triggered spikes in individual pyramidal neurons in awake mice. a Schematic view of activity windows to calculated auto- and cross-correlations. **b** Holographically triggered TC spikes are novel, as evidenced by their zero autocorrelation during ongoing activity. In contrast, autocorrelations remain high for other neuron categories, except NegR, due to spike failure during the response. **c** Ongoing TC spike fluctuations positively correlate with all neuron groups. However, evoked TC spikes selectively correlate positively with PosR, show no correlation with NonR, and correlate negatively with NegR. **d** Scaling for ongoing fluctuations in TC with respect to all other groups. Note limited range in spontaneous TC count fluctuations of <10 spikes/132 ms. **e** Robust scaling for novel spikes in TC with respect to PosR but not NonR or NegR. **f** Scaling of population spike count for each neuron category separately and combined (*black*). **g** Strong positive scaling for PosR remains even when significance level alpha is greatly reduced. Change in scaling exponent as a function of alpha per neuron (*avg; solid lines*) and population (*sum; dashed lines*) for each group. **h** PosR are predominantly located within a 100 μm radius of the TC but also distribute throughout the network as alpha decreases. **i** Relative number of neurons per category changes with alpha. Note that PosR and NegR make up the majority of the observed network at the lowest significance level at which robust scaling is still observed. **j** The Fano Factor (FF) remains unchanged for PosR and NonR despite significant scaling in PosR ($\alpha = 2.5\%$). *Opaque bars*: Mean spike count corrected FF (see Methods). **k** Population FF also shows no change across categories. *Shaded areas* (d – f) and error bars (b, c, j, k): SD. When comparing correlations (b, c) and FF (j), 1, 2 & 3 stars indicate $p < 0.05$, 10^{-3} & 10^{-6}, respectively, using Wilcoxon rank sum test.

150 The corresponding recruitment of both PosR and NegR from the NonR pool (Fig. 2g–i) suggests
151 that novel spikes are transmitted across the network via multi-synaptic pathways and concomitant
152 increases as well as decreases in spiking as recently described when stimulating groups of pyramidal
153 neurons simultaneously[7]. The engagement of a large number of neurons distributed over broad spatial
154 regions when stimulating a single pyramidal neuron contrasts with expectations from anatomy and
155 single cell physiology regarding the efficacy of transmitting single action potentials.
156 A reduction in spiking variability, measured by the Fano factor (FF; variance-to-mean spike
157 count), is a well-documented response to sensory stimulation[34] and may underlie the robust scaling
158 observed with TC stimulation. On the other hand, simultaneous holographical stimulation of groups of
159 neurons exhibits variable spike counts in individual TCs through recurrent circuit dynamics[7], which
160 should counter-balance FF decreases in the network. We found that repeated holographic stimulation
161 reduced the FF in TC neurons as expected from the increase in regular driving, however, the FF for
162 PosR and NonR remained unchanged, even after accounting for differences in mean spike count[35] (Fig.
163 2j). Similarly, no change in FF was observed for PosR and NonR population responses (Fig. 2k). To
164 investigate whether variability in TC spike triggering masked changes in FF for PosR and NonR, we
165 analyzed subgroups of TC trials with differing FF, population activity, and post-response time windows.
166 However, the FF remained consistently high and unaltered for both groups across all conditions
167 (Supplementary Figs. 5, 6).
168 Our findings demonstrate that novel spikes in a single pyramidal neuron elicit significant scaling
169 responses in a large group of neighboring neurons, while preserving a fluctuation-dominated regime.
170 This indicates that cortical network in vivo operate in a fluctuation-dominated regime in which local
171 fluctuations exhibit responses in line with critical scaling[28,36].
172

173 **Temporally accurate information on the origin of novel spikes distributes throughout the**
174 **network**

175 We next demonstrate that widespread spike count changes in response to novel spikes encode crucial
176 information about their origin, which is rapidly and transiently distributed across the cortical network. In
177 n = 7 experiments, up to 10 TCs were stimulated in a semi-random order (100 ms each, with 2–10 s
178 intertrial intervals; Fig. 3a). The origin of these novel spikes was successfully decoded from the activity
179 of the non-driven neurons using two machine learning approaches: XGBoost[37] (XGB) and Random
180 Forest[38,39] (RF; see Materials and Methods).
181 Decoding accuracy and F1-scores exceeded 90% for both algorithms when utilizing the full
182 network excluding TC neurons (Fig. 3b; Supplementary Fig. 7a), with a positive correlation between F1-
183 scores and the number of trials that elicited spikes in TCs (Supplementary Fig. 7d). Importantly,

184 between 10–70% of best decoding neurons needed removal for accuracy to drop to chance level (Fig.
185 3c). In a representative experiment (Fig. 3d), F1-scores of TCs dropped to chance levels after removing
186 >70% of the best-encoding neurons. On average, 20–30% of the best-encoding neurons were sufficient
187 to achieve high decoding accuracy, regardless of the algorithm used (Fig. 3e; Supplementary Fig. 7c).

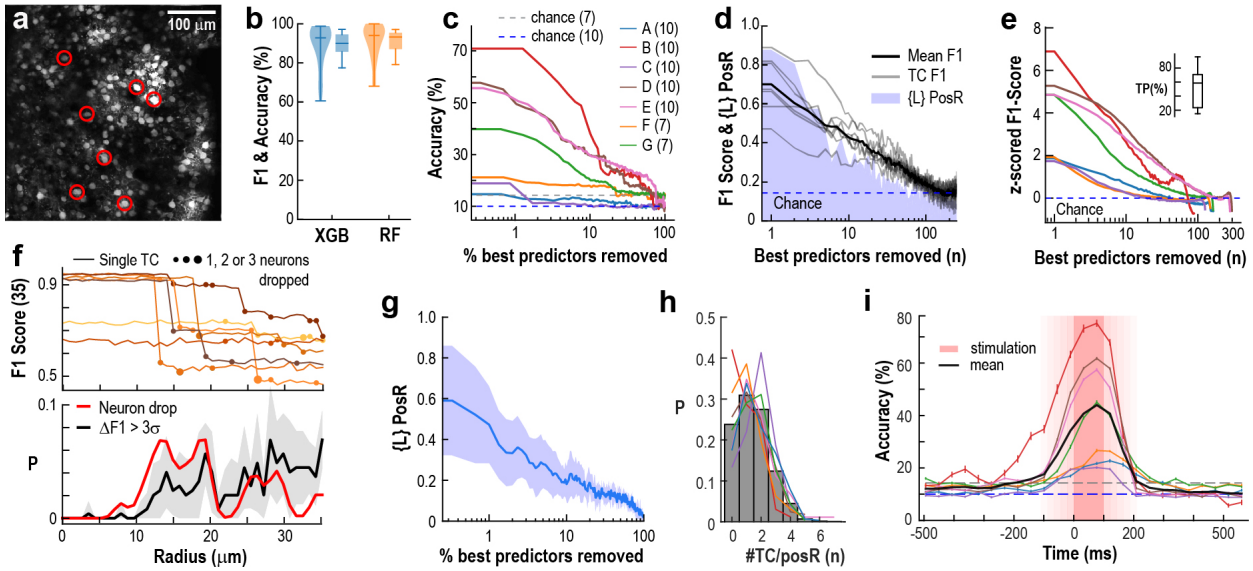

Fig. 3 | Information on the origin of novel spikes propagates widely and transiently in superficial layers 2/3 of the awake and resting mouse. a Example field of view with targeted TCs (*circled*) and network neighborhood (mean baseline activity). **b** High decoding accuracy (*violin plot*) and F1 scores (*box plot*) for identifying TC origin from network responses using XGBoost (XGB) or Random Forest (RF; n = 7 experiments; chance level 10 – 14%). **c** Removing 10–70% of best decoding neurons (ranked by Shapley values) drops accuracy to chance (*dashed lines*; A – G experiments; *brackets*: # TCs). **d** Distributed TC spike information: up to 100 top decoding neurons must be removed to reach chance (single experiment). F1-score of individual TC and probability of removing a PosR (*purple area*). **e** Mean drop in F1-score across experiments (XGB). *Inset*: Average percentage of best decoding neurons removal to reach chance. **f** Radius-dependent exclusion confirms spatially restricted TC stimulation, excluding neighbors. *Top*: F1 drop vs. radial exclusion from TCs (single experiment). *Bottom*: ΔF1 (*black*) summarizes probability of F1 changes >3σ (SD: *grey*) and probability of neuron drop (*red*; all experiments). **g** Summary of likelihood, L of dropped neuron being PosR for all experiments. **h** Individual neurons can qualify as PosR to multiple TCs. Average probability distribution for the number of TCs a neuron is categorized as PosR across experiments (*lines*). **i** Novel spike Information is transient: decoding success exceeds chance (*dashed lines*) only when the response window (*pink areas*) overlaps with the stimulation period (0–100 ms).

188

189 Positive spike count changes (PosR; α = 2.5%) contributed significantly, accounting for 30–60%
190 of decoding success (Fig. 3d, g). As a further control, we performed a radius exclusion analysis which
191 demonstrated direct stimulation of non-TC cells did not influence decoding statistics. Excluding neurons
192 within <10 µm of a TC had no effect on performance, but stepwise removal of neighboring non-TC
193 neurons progressively reduced decoding accuracy (Fig. 3f).
194 Individual neurons responded significantly to the stimulation of up to five different TCs,
195 suggesting that they are capable of contributing to the decoding of multiple TCs, with significant overlap
196 in the functional networks that encode where novel spikes originate (Fig. 3h). Information about these
197 novel spikes faded quickly once the stimulus ended (Fig. 3i), aligning with the short-lived response
198 profile in all neurons (cf. Fig. 1c). The increased decoding accuracy before stimulation can be attributed
199 to temporal averaging (132 ms) and the use of Deep-Interpolation[40], which reduces noise to improve
200 accuracy but slightly broadens the time of responses without impacting the overall results
201 (Supplementary Fig. 7b).
202 These findings demonstrate that the cortical superficial layers can reliably and briefly transmit
203 precise information about the timing and source of novel spikes, highlighting a robust, distributed
204 mechanism for processing unexpected inputs across the neural network.
205

206 **Novel spikes scale network responses during the fluctuation dominated regime of ongoing**
207 **neuronal avalanches**

208 For many neurons, the spike count in encoding of novel spikes showed higher variability than expected
209 from a Poisson process (Fig. 1), with Fano factors similar to those observed during ongoing neuronal
210 activity (Fig. 2). This variability extended to the population of subclasses, such as PosR. To better
211 understand this fluctuation-dominated activity regime, we studied its statistical properties in relation to
212 novel spike encoding.
213 Holographic stimulation occurred during large fluctuations in ongoing activity (Fig. 4a),
214 measured as continuous population activity above a small threshold. These suprathreshold periods
215 exhibited heavy-tail distributions in size (summed spikes), and duration as described previously for
216 neuronal avalanches[29,41] (Fig. 4b). Notably, when correcting for subsampling biases using temporal
217 coarse graining, mean avalanche size scaled quadratically with avalanche duration – a hallmark of
218 parabolic avalanches – which includes avalanches lasting up to ~0.7 s, accounting for 87% of all
219 avalanches and ~20% of all spikes during ongoing activity (Fig. 4c, d). Avalanches exceeding >1 s
220 exhibited linear scaling close to 1, representing activity too large to resolve within our field of view[29,41,42].
221 Notably, novel spikes influenced the timing of ongoing avalanche initiation and termination, due to
222 added population activity during stimulation (Fig. 4e).

223

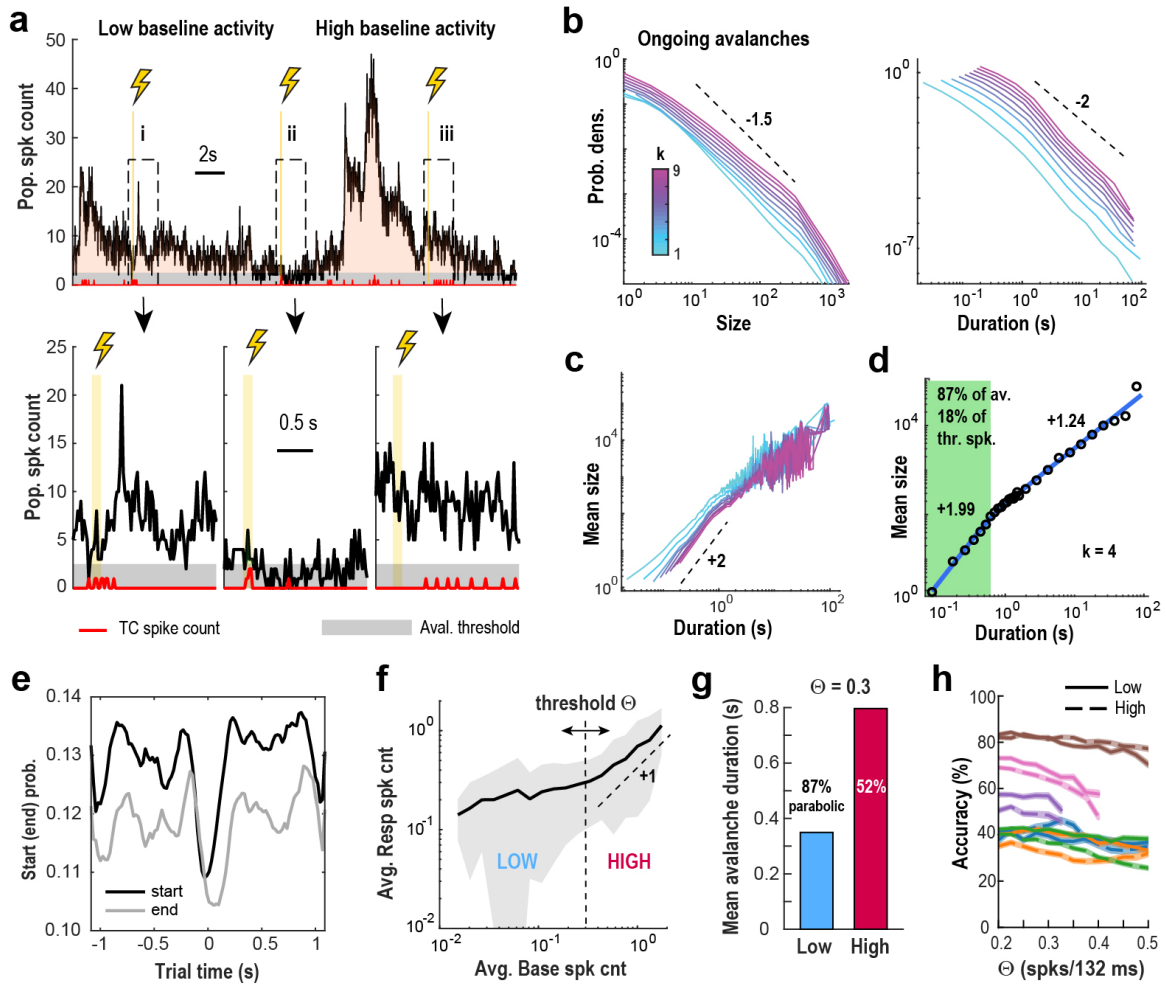

Fig. 4 | High decoding accuracy of novel spikes occur during scale-free avalanche dynamics despite highly fluctuating levels of baseline activity. a *Top*: Population activity in visual cortex of the awake mouse exhibits large fluctuations during quiet resting. *Bottom*: Zoomed in view of population activity in response to 3 (i – iii) holographic stimulations of a single TC. *Vertical lines*: TC stimulation. *Red line*: TC spike count. *Grey stripe*: Population threshold for avalanche detection. Shown is the population spike count (excluding TCs) per 22-ms frame. **b** Suprathreshold contiguous fluctuations in population activity exhibit the characteristic hallmarks of neuronal avalanches. Avalanche size (*left*) and duration (*right*) distributions as a function of the temporal coarse-graining factor *k*. **c** Scaling of avalanche dynamics as a function of temporal coarse-graining k. **d** Approximately 87% of avalanches are parabolic in nature, with durations <0.7 s, containing about 18% of thresholded spikes. Summary scaling of parabolic avalanches is shown for durations up to ~0.7 s ($k = 4$). **e** Holographic stimulation influences avalanche initiation, with a decreased likelihood for avalanche start and end during stimulation. **f** Mean response spike count scaling as a function of mean baseline spike count for non-TC neurons. This analysis reveals a low baseline activity regime (mean baseline spike count < ~0.3), in which responses are mostly independent from base activity, distinct from a high baseline activity regime in which response activity can be predicted from base. **g** Mean avalanche duration is more than double for avalanches that start during LOW base trials compared to HIGH. 87% of all LOW avalanches are parabolic (scaling of $\chi = 2$), whereas only ~52% of HIGH avalanches are parabolic. **h** Decoding accuracy remains largely unchanged when obtained using only LOW or HIGH baseline activity regimes, regardless of the threshold used to define the two regimes. Overall accuracy for Low base trials (*solid lines*) and High base trials (*dashed lines*) for each dataset (same color code as in Fig. 3), as function of the threshold used to define Low and High base trials.

Decoding of novel spikes remained remarkably robust across the avalanche scaling regime despite large fluctuations in baseline activities. For baseline activity below a threshold ($\Theta < 0.3$ spikes/132 ms), response spike count scaled only moderately, while for $\Theta > 0.3$ spikes/132 ms, the scaling approached 1, the latter indicating strong correlation between pre-stimulus and stimulus spike counts (Fig. 4f). This enabled classification of baseline activity into a low- and high-activity regime respectively which prominently featured parabolic avalanches (Fig. 4g). Importantly, novel spike encoding differed by less than 4% in accuracy on average between these two regimes independent of Θ (Fig. 4h, Supplementary Fig. 7e).

Discussion

Efficient communication of novel neural signals is vital for processing surprises and guiding future actions. Using an all-optical approach in awake, resting mice, we demonstrated that holographically introducing action potentials in a single L2/3 pyramidal neuron rapidly activates widespread responses in the surrounding cortical network, encoding the novel stimulus' origin. Remarkably, these responses scaled robustly and were efficiently decoded amidst ongoing, large fluctuations in network activity organized as scale-invariant, parabolic neuronal avalanches. This high susceptibility to local perturbations[27,28], with a scaling exponent of ~0.2–0.3, highlights critical dynamics as a cornerstone of cortical processing, offering key insights into brain function.

Our findings challenge a longstanding discussion on cortical coding fueled by the intricate statistical anatomy of the cortex and its synaptic connections. Pyramidal neurons in associative layers rarely establish synaptic connections with their neighbors[19-23]. These excitatory connections are relatively weak, prone to failure, and decay within milliseconds[22,43]. This combination of sparse and weak connectivity makes it unlikely that a spike in a single neuron could propagate reliably in the surround network. To address this, most cortical codes rely on activity patterns that amplify synaptic impact on postsynaptic pyramidal neurons.

For instance, coincident activation of numerous synapses from diverse neurons converging onto a postsynaptic target enhances the likelihood of activity propagation, favoring coding models based on local synchrony, such as synfire chains[44,45], waves[46,47] or phase-locked oscillations[48,49]. Alternatively, repeated or burst firing of individual neurons[12,50], strong synaptic connections[51], subthreshold priming by background activity[15,52] supported by subcellular amplification mechanisms such as short-term synaptic facilitation[53,54] and non-linear dendritic processing[55] can dynamical increase individual connection strength supporting rate-based coding.

Our findings do not support a dichotomic separation into synchrony vs. firing rate separation in the propagation of neuronal activity (see also [24,56]). We show highly efficient scaling of novel spikes within the cortical neighborhood from single to multiple action potentials delivered within 100 ms. This suggests that neither tight synchrony nor repeat firing is strictly necessary for effective encoding of novel spikes. This conclusion is in line with findings that spike counts over 100 ms predict behavior independent of considerations of synchrony at the millisecond level[57]. By emphasizing the sufficiency of a few action potentials in cortical codes, our results thus challenge existing paradigms and highlight a minimalist yet efficient mechanism for cortical information processing supporting the prominence of sparse, single action potential firing found in vivo for associative layers[58].

Our findings demonstrate the remarkable impact of just a few action potentials amid the thousands of spikes generated every second in the awake brain's cortical neighborhood. In a cortical volume with a neuronal density of ~100,000 neurons per cubic mm and a connectivity radius of 0.2 mm[19], the local spherical neighborhood of ~3,300 neurons exhibiting a mean firing rate of ~1 Hz at rest (*cf*. Fig. 1d) produces approximately 3,300 spikes per second that could influence a single neuron's state. This apparent spike abundance might suggest that a few added action potentials have negligible influence. However, our results challenge this assumption, showing that introducing 1–7 novel spikes in a randomly chosen, single pyramidal neuron, not synchronized with neighboring activity, can have extensive spatial reach and convey significant information, even within the highly fluctuating activity of the ongoing network. Given our 0.45×0.45 mm field of view and ~170 imaged neurons (*cf*. Fig. 2i), we sample ~5% of this neighborhood (<170/3300). At a conservative significance level of $\alpha = 2.5\%$, we observed ~23 PosR per TC (1221/54; Fig. 1d), which translates to more than 450 neighboring neurons significantly *increasing* their firing within tens of milliseconds in response to our holographic stimulation. This estimate, however, is likely highly conservative as lowering alpha further increases the number of neighboring neurons with detectable changes in spiking, as confirmed by our decoding results. Notably, reducing α, also reveals a role for local inhibition in intracortical circuits[25,26]. This adjustment increasingly recruits both positive and negative responses from the pool of previously non-significant responders. These recruitments are most likely composed of a mixture of direct (excitation, inhibition) as well as indirect (disfacilitation, disinhibition) local circuit interactions[4,7], while preserving the general scaling relationship (cf. Fig. 2). Simulations have found that in such a fluctuation-dominated but relatively balanced regime, a reduction in membrane conductance due to increased synaptic bombardment still enables neurons to generate few spikes in response to rapid changes in synaptic input[17].

287 The importance of critical dynamics for sensory cortical networks has been argued from the
288 point of view of optimal decoding of stimulus intensities through maximization of the dynamic range[59]. In
289 that context, a critical network is expected to produce response-input curves that scale as a power law,
290 with exponents that are typically much smaller than one[28]. The study of psychophysics has
291 demonstrated that psychological value scales with stimulus intensity as a power law with <1 exponents,
292 a result known as Stevens' law of psychophysics[60]. Therefore, it has been argued that the origins of
293 Steven's low exponents for response curves might originate precisely at this critical networks' ability to
294 amplify low-intensity stimuli and thus respond to a wide range of stimulus intensities[61]. We were able to
295 show that *in vivo* sensory cortical networks do display low-exponent, power-law behavior for their
296 response to varying stimuli intensity (as proxied by the number of spikes evoked in a target cell during
297 stimulation). This is in line with predictions from critical dynamics, with the observed exponents closely
298 matching the expected value (0.285) for a two-dimensional directed percolation system[28].

299 Our decoding analysis provided important insights about the fine-grained nature of this
300 communication of novelty. First, strongly decoding neurons were found in the immediate neighborhood
301 of TCs supporting a spatial weighing in the response, in line with expectations from the local, synaptic
302 connectivity statistics of pyramidal neurons. On the other hand, a large fraction of neurons with high
303 decoding contribution did not fall into the PosR category or were located at long distances from the TC,
304 supporting the contribution of indirect pathways. This also de-emphasizes reliance on distinct, non-
305 overlapping network connectivity.

306 The ability of PosR neurons to contribute significantly to the decoding of multiple TCs is in line
307 with the spatial overlap of neuronal populations encoding different stimuli and their temporal separation.
308 Our findings align with the notion that cortical networks are organized to maximize coding efficiency and
309 redundancy, where overlapping populations can fluctuate in their response patterns to encode different
310 stimuli[62,63]. The rapid decay found for the encoding of novel spikes further underscores this dynamic,
311 ensuring that novel signals do not disrupt ongoing network activity but still convey novel information
312 effectively within the constraints of the temporal and spatial coding architecture described for e.g. visual
313 stimuli of the primary visual cortex in the awake mouse[64].

314 Our findings of maintained high Fano factor in evoked responses is in contrast to quenched
315 variability demonstrated in response to sensory stimuli[34]. This difference may arise because single-
316 neuron stimulation introduces a smaller perturbation than sensory stimulation, which in the awake state
317 is dominated by inhibition[25], affecting response variability. Early studies in anesthetized animals[18] (e.g.
318 in the visual cortex of cats) demonstrated that trial-by-trial variability in stimulus responses can be
319 approximated as average response overlaid on a correlated, variable background. In the awake state,

our observation of consistently high FF values for responses in the presence of scale-invariant parabolic avalanches indicates the need for a conceptual approach that bypasses the reliance on averaging. Avalanches emerge in superficial layers of cortex when animals recover from anesthesia[65,66], exhibit high neuronal selectivity[67,68] and spatiotemporal order[69-73] characterized by power law statistics with exponents ≤2 that is, averages are not defined and variability is high. We demonstrate that decoding of novel spikes is similar across the fluctuation dominated avalanche regime (Fig. 4).

Our results reveal the efficient communication of single spikes within the scale-invariant, critical-state dynamics of cortical networks, where synchronized fluctuations are neither overly constrained nor entirely random. We propose this remarkable sensitivity of the mammalian cortex, to efficiently disseminate novel information from individual neurons, underscores the fundamental role of critical dynamics in cortical communication and computation.

Materials and Methods

Animal surgery

All procedures were approved by the NIH Animal Care and Use Committee (ACUC) and experiments followed the NIH *Guide for the Care and Use of Laboratory Animals*. Mice were obtained from Jackson labs, bred inhouse with C57BL/6 backgrounds (Jackson Laboratory) under a reversed 12:12 hr light/dark cycle. Chronic 2PI imaging in adult (>6 weeks) mice was enabled by using a head bar in combination with a cranial window placed centered at ~2.5 mm from the midline (right hemisphere) and ~1 mm rostral to the lambdoid suture and consisting of a stack of circular glass cover slips using established protocols[74]. Mice were injected with a 7:1 mixture of a viral construct to express jGCaMP7s[75] and ChrimsonR[76] in pyramidal neurons using the CaMKII promotor. A total of 2 – 3 injections of virus (100 – 400 nL; <1 µL in total; 10^{13} vg/mL; pGP-AAV-syn-jGCaMP7s-WPRE AAV9 & pAAV-CamKIIa-ChrimsonR-mScarlet-KV2.1, Addgene) were administered into the right hemisphere. Chronic 2PI started after >2 weeks in identified V1 at a depth of ~100–200 µm.

Identification of V1 maps

Retinotopic maps of V1 and higher visual areas (HVAs) were generated for all mice prior to recording using published protocols[77,78]. Briefly, awake, head-fixed mice faced with their left eye a 19” LCD monitor placed at 10 cm distance and tilted 30º towards the mouse’s midline. Using Psychophysics toolbox[79], contrast-reversing, spherically corrected checkerboard bars were drifted across the screen vertically (altitude) and horizontally (azimuth) for each of the four directions (30 repeats per direction).

352 Simultaneous wide-field imaging (Quantalux, Thorlabs) captured jGCaMP7s fluorescence, which was
353 averaged for each direction. Altitude and azimuth phase maps were calculated by phase-wrapping the
354 first harmonics of the 1D Fourier transform for each of the four averages and subsequently subtracting
355 the maps of the opposite directions[78]. Sign maps were generated by taking the sine of the angle
356 between the gradients in the altitude and azimuth maps and processed[77]. Borders were drawn around
357 visual area patches and overlaid onto anatomical reference images to identify V1.
358

359 **Holographic stimulation of single neurons**

360 Holographic stimulation[80] was done by manually selecting individual pyramidal neurons as target from
361 the two-photon image of the field of view in both red and green channels. Neurons that express the
362 opsin (ChrimsonR, with mScarlet tag) were selected for stimulation. Based on the selected targets, a
363 map of top-hat patterns with diameter of 10 µm was used to generate the hologram on the Spatial Light
364 Modulator (SLM, Meadowlark, LCoS high resolution 1920×1152 phase modulator). Light from the
365 laser/OPA system (Carbide/Orpheus-F – Light Conversion, λ = 1064 nm, repetition rate = 600 kHz,
366 pulse width <100 fs) was expanded (4x) to fill the area of the SLM (8 mm × 8 mm). The hologram on
367 the pupil plane was shrunk to fit the size of the Galvo-Galvo scanners (~3 mm diameter) and form the
368 desired pattern of top hats after the objective lens (Nikon 16X, working distance = 3mm and effective
369 focal length = 12.5 mm) on the selected targets. Each target neuron was continuously stimulated by the
370 top-hat beam shape for 100 ms for a total of ~100—150 trials per experiment, with an interval of 2 s (10
371 s in some recordings) between trials. Power at target neurons ranged from ~2.5 – 10 mW.
372

373 **2PI imaging, pre-processing pipeline and meta data collection**

374 For standard 2PI, images were acquired by a scanning microscope (Bergamo II series, B248, Thorlabs
375 Inc.) coupled to a pulsed femtosecond Ti:Sapphire 2-photon laser with dispersion compensation
376 (Chameleon Discovery NX, Coherent Inc.). The microscope was controlled by ThorImageLS and
377 ThorSync software (Thorlabs Inc.). The wavelength was tuned to 940 nm to excite jGCaMP7s. Signals
378 were collected through a 16× 0.8 NA microscope objective (Nikon). Emitted photons were collected
379 through a 525/50 nm band filter using GaAsP photomultiplier tubes. The field of view was ~450×450
380 µm. Imaging frames of 512×512 pixels were acquired at 45.527 Hz by bidirectional scanning of a 12
381 kHz Galvo-resonant scanner. Beam turnarounds at the edges of the image were blanked with a
382 Pockels cell. The average power for imaging was <70 mW, measured at the sample.
383 The obtained tif-movies in uint16 format were rigid motion-corrected via the python-based
384 software package '*suite2p*'[81]. Registered images were further denoised using machine-learning based,
385 deep interpolation[40] (see below) and then semi-automatically processed by suite2p for ROI selection

386 and fluorescence signal extraction. For each labeled neuron, raw soma and neuropil fluorescence
387 signals over time were extracted for each ROI. Spiking probabilities were obtained from neuropil-
388 corrected fluorescence traces ($F_{corrected} = F_{ROI} - 0.7*F_{neuropil}$) via MLspike (https://github.com/MLspike),
389 utilizing its autocalibration feature to obtain unitary spike event amplitude, decay time, and channel
390 noise for individual ROIs.
391
392 *Deep-interpolation*
393 Deep-interpolation[40] (Deep-IP; https://github.com/AllenInstitute/deepinterpolation) removes independent
394 noise by using local spatiotemporal data across a noisy image stack of $N_{pre} + N_{post}$ frames to predict, or
395 interpolate, pixel intensity values throughout a single withheld central frame. The deep neural network
396 is a nonlinear interpolation model based on a UNet inspired encoder-decoder architecture with 2D
397 convolutional layers where training and validation are performed on noisy images without the need for
398 ground truth data. As described previously in detail[68], after rigid motion correction, individual denoised
399 frames were obtained by streaming one 60-frame ($N_{pre} = N_{post} = 30$ frames) registered, image stack
400 through the provided Ai-93 pretrained model[40] for each frame to be interpolated. At an imaging rate of
401 ~45 Hz, these 60 frames correspond to a combined ~1.3 seconds of data surrounding the frame to be
402 interpolated.
403
404 **Postprocessing pipeline**
405 Our postprocessing pipelines were custom-written in Matlab (Mathworks) and Python
406 (www.python.org). Some routines utilized NumPy (https://numpy.org/) and Matplotlib
407 (https://matplotlib.org/).
408
409 *Stimulus response measurement*
410 Unless stated otherwise, spike count over a window of 6 imaging frames (~132 ms) starting at the
411 stimulation onset was used as a measure of the response to holographic stimulus of each target cell for
412 all cells. This was compared to the baseline count, defined as a 6-frame window starting ~264 ms
413 before stimulus onset. Due to difficulties and limitations of spike deconvolution of calcium traces, some
414 parts of the time series resulted in artificially high spike rates. To avoid artificial increase of variability
415 measures due to these artifacts, we introduced an outlier removal procedure in which trials with spike
416 count above 10 standard deviations over the mean are removed from the analysis. This procedure
417 resulted in <0.1% trials removed, across all neurons for all experiments.
418
419 *Target selection and exclusion*

Up to 25 target cells were visually selected based on expression and location in the field of view (cells close to the edges were avoided) for each experiment. Not all targets were responsive to stimulation. Targets in which fewer than 20% of the trials evoked a spike count above the 91% percentile of its baseline count were excluded from the analysis. This procedure resulted in 54 target cells across 16 experiments from 6 mice being considered out of 193 targets attempted across 33 experiments from 11 mice. We estimate an average of 46.3 ± 17.9 ChrimsonR-labeled cells per field of view, which translates to an average density of labeled cells of ~2.3×10^{-4} cells per μm^2. This sparse labeling facilitates the holographic stimulation of individual targets (see Supplementary Fig. 3).

Definition of significant responders

Cells with significant response to each target's stimulation were defined as those whose spike count distribution was significantly different from its baseline count distribution. Specifically, we used a z-test to compare the stimulus response spike count to the average and standard deviation of the baseline count for each non-target cell. A cell was defined as a positive responder if the z statistic is above the highest 2.5% of the distribution and as a negative responder if the z statistic is below the lowest 2.5%. Otherwise, the cell is classified as a non-significant responder. This procedure is done for each target stimulated in an experiment separately. Therefore, in experiments where multiple targets were selected, each non-target cell is tested for significance of its response to each target's stimulation, possibly being a significant responder for some targets and non-significant responder to others (see Fig. 3h).

Fano Factor calculation and significance

Fano Factor was calculated as usual, for each cell separately, by dividing the variance of their spike count by the mean of their spike count across trials. To correct for changes in firing rate across conditions[35], we introduced a procedure in which the window used to measure the spike count during stimulation varied from 1 to 9 frames (~22 ms to 198 ms), starting at the onset. The window length was determined by minimizing the normalized difference between the mean baseline and stimulus counts. Cells for which this difference was above 20% were excluded from the analysis. This procedure resulted in less than 30% of cells removed, on average, across the non-target cells and an average of 65% of targets removed (minimum of 13% or 7 targets considered). Values were reported as mean ± error over the mean across cells, unless stated otherwise. Significance of Fano Factor changes across conditions was obtained by employing the Wilcoxon rank sum test at a significance level of 0.05 (p-values reported in Results section and figure legends).

454 *Trial separation and controls*
455 To control for different conditions affecting the variability, the Fano Factor was recalculated and
456 compared using a subset of trials. To control for target cell response variability affecting non-target
457 cells, we separated trials into low target count trials and high target count trials. We defined low count
458 trials as those for which the target cell produced a spike count during stimulation that was above the
459 91st percentile of the baseline count distribution and up to twice that number of spikes, whereas high
460 count trials were any trial with count above that limit. To control for the influence of ongoing fluctuation
461 of the network activity we separated trials into low and high population baseline count, defined as trials
462 for which the population count during baseline was lower than the 25th percentile of its distribution or
463 higher than 75th percentile, respectively. To control for temporal influence of the responses to the
464 stimulus, we defined two consecutive 6-frame windows, centered at the peak of the target's average
465 response to the stimulus (2—3 frames after onset), as early and late response windows.
466
467 *Correlation analysis*
468 Spike counts across trials were compared by computing correlations across time (autocorrelation,
469 calculated using the spike counts over pairs of windows separated by a temporal lag of 132 ms) and
470 across cells (comparing spike counts of targets *vs* non-targets). Values are reported as mean ± error
471 over the mean. Significance of correlation changes across conditions was obtained by employing the
472 Wilcoxon rank sum test at a significance level of 0.05 (p-values reported in Results section and figure
473 legends).
474
475 **Decoding Analysis**
476
477 *Classification model selection, performance metrics, and data preprocessing*
478 In our prediction and classification scheme, we used target neuron ensembles as "classes" and the
479 activity of the responding/non-target neurons as the "features". As described in Stimulus response
480 measurement section, we use spike count over a window of 6 imaging frames as a feature value for
481 each neuron. For the temporal analysis, this window is offset relative to stimulus onset, as described
482 below. In a preliminary analysis, we compared several machine learning strategies and found that the
483 ensemble methods of boosting (XGBoost[37]) and bagging (scikit-learn[82] Random Forest classifier)
484 performed best to several other common classification schemes such as Logistic Regression, Naive
485 Bayes, Neural Networks, and Support Vector Machines. These two approaches yielded the highest
486 accuracy and were then applied to all of our analyses presented in this work. In all cases we split the
487 data samples randomly so that 80% was used for training and 20% for testing. We repeat this split 100

times and from these report the mean and standard errors of our metrics. As metrics we use overall accuracy, per-class recall and precision, as well as F1-scores (harmonic mean of recall and precision). For the results in Figs. 3c, h we use all data and all trials, but for others we performed additional pre-processing, before running classification.

Since not all trials were equally successful in eliciting spikes from target cells, for all other decoding analysis we selectively filtered trials and targets, with a criterion that the target neuron had to produce at least one spike across any of the six frames after the onset of stimulation. We then selected valid targets as those that spiked on at least half of their trials. Thus, non-significantly driven TC (based on conservative response spike count) excluded some TC in the spike count analysis which nevertheless had significantly F1-score in the decoding task (gray TC in Supplementary Fig. 7a). To characterize feature importances and interpret our classification schemes we used Shapley analysis[83], as described below.

Radius Analysis

For each target neuron, we implemented an exclusion zone based on the distance from the target neuron's soma, *r*. We progressively increased *r*, and the neurons/features falling within this distance were systematically eliminated from the feature matrix, enabling quantification of the relationship between F1-score degradation and exclusion zone radius for individual target neurons. We computed the probability distribution of any feature neuron being excluded, as a function of distance, $P_{ex}(r)$. Specifically, we aggregated the frequency of neuron eliminations at each radius across all datasets and normalized by the total number of exclusions.

The spatial dependency of predictive performance was characterized by analyzing the differential changes in F1-score across the range of exclusion radii. For each target neuron across all datasets, we identified the radius at which the decrease in F1-score first exceeded three standard deviations below the mean rate of change. These radii were averaged across datasets and smoothed using a Gaussian kernel ($\sigma = 1$) to obtain an estimate of the spatial scale of predictive influence.

Neuron Drop Analysis and Positive Responder Probability

To evaluate the distributed nature of neural information and assess the robustness of our decoding framework, we conducted an iterative feature elimination analysis for each target neuron across all datasets. For each iteration, including initial model fitting, we use Shapley values (employed using SHAP package: SHapley Additive exPlanations[84] to quantitatively rank feature neurons based on their predictive contribution for a given target neuron. Through sequential elimination of the highest-ranked feature neurons and subsequent model retraining, we systematically assessed how the removal of

informative neurons impacted decoding performance. This iterative process of SHAP-guided feature elimination and model reconstruction was repeated until a single neuron remained. At each iteration we recorded F1-score, precision, and overall accuracy and the entire procedure was replicated one hundred times, utilizing different out-of-bag random selection of training and testing sets.

To characterize the relationship between feature importance and significant responders, we quantified the probability that eliminated neurons exhibited significant responses. For each target neuron, we constructed a binary vector corresponding to the sequential elimination order, where entries were assigned values of 1 or 0 based on whether the eliminated neuron was a significant responder. These binary sequences were averaged across all iterations of the elimination procedure to obtain target-specific probabilities and then averaged across all target neurons.

Temporal profiles of the prediction accuracy

To further characterize our holographic stimulation data we explored the accuracy of our prediction scheme as a function of time. This procedure allowed us to study how long the information about the origin of stimulation persists in network. Note that the prediction scheme is a more stringent requirement than studying only the causal effects of stimulation, since even though the activity after the stimulation can reverberate in a network for a long time, identifying the node that initiated it is more challenging.

We assessed the temporal course of the prediction accuracy across datasets, each with different levels of responsiveness of the targets. We varied the size of our response window (2 through 8 frames) and then moved it in steps of 2. The main results are present in Figure 3h. The fading “pink” rectangles indicate the amount of data used from the stimulation region (100 ms) window, so that the fully white regions use data strictly before or after stimulation is over. Note that the bins and the stimulation region are not perfectly aligned, as the trigger for the stimulation was independent from the image scanning raster. We define the reference bin 0 as the first bin which fully overlaps with the stimulation.

Avalanche analysis

Continuous epochs of suprathreshold population activity

Continuous periods of population activity were identified by applying a threshold Θ on the population activity $p(t)$, the sum of the spikes from all neurons at a given time t, such that:

$$p_{\Theta}(t) = \begin{cases} p(t) - \Theta & p(t) > \Theta \\ 0 & p(t) \leq \Theta \end{cases} \quad (1)$$

This procedure is known as soft-thresholding and was employed for all analysis unless otherwise stated. For a given recording $p(t)$ and coarse-graining value k, the dependence of the number N of epochs on the threshold Θ, N(Θ) was obtained for a range of thresholds $\Theta \in [\Theta_1, \Theta_2]$ such that Θ_1 was low enough that it removed no population activity from the time course and Θ_2 was high enough that it would remove all population activity from the time course. The function N(Θ) was typically well-approximated by a log-normal distribution and a corresponding fit yielded shape parameters μ and σ. The threshold used in the analysis for all recordings and coarse-graining factors was chosen such that $\Theta = \mu$ and estimated for each k. See Capek & Ribeiro et al.[68] for more details.[30,69,85,86]

Temporal coarse-graining

A temporal coarse-graining operation was applied to the thresholded population activity $p_\Theta(t)$. For a given temporal coarse-graining factor k an ensemble of K different coarse-grained time series $p_k^0(\tau), p_k^1(\tau), \ldots, p_k^{K-1}(\tau)$ was arrived at through the following method:

$$p_k^j(\tau) = \sum_{i=k\tau+j}^{k(\tau+1)+j-1} p_\Theta(i) \quad for\ \tau \in [0,1,\ldots,\left\lfloor\frac{T-j}{k}\right\rfloor] \tag{2}$$

For each time series $p_k^j(\tau)$, epochs were extracted by finding pairs (τ_1, τ_2) such that $p_k^j(\tau_1) = 0$, $p_k^j(\tau_2) = 0$ and $p_k^j(\tau') > 0$ for all $\tau' \in [\tau_1 + 1, \ldots, \tau_2 - 1]$. The size of the epoch is given by $S = \sum_{i=\tau_1}^{\tau_2} p_k^j(i)$ and its corresponding duration given by $\tau_2 - \tau_1 - 1$. For a given ensemble of coarse-grained time series, all epochs were combined.

Scaling curve fit

For more precise evaluation of χ_{sh} and χ_{lg}, we introduced the following fitting function:

$$S(d) = \frac{C d^{\chi_{sh}}}{(1+(d/\Phi)^\gamma)^{(\chi_{sh}+\chi_{lg})/\gamma}} \tag{3}$$

This function is a double power law with initial slope χ_{sh}, transitioning to a second slope χ_{lg} at around the point $d = F$. The parameter g controls how abruptly that transition happens and has been fixed at 4 for all the curves presented. The other parameters were free to adjust to the data, and all fits were performed in log-space, i.e., the log(S(log(d)) was fit to the log of data (taking the log of both average sizes as well as durations).

Data availability

The preprocessed imaging data used in this study are available in the general repository Zenodo using the following access DOI:TBD (Ref. [87]). The source data for all figures and supplemental figures in this

study are provided for this paper.

Code availability

Computer code used in this study is available at the following github link: TBD.

Acknowledgements

We thank Craig C. Stewart and members of the Plenz lab for help with animal surgery, animal care. This research was supported by the Division of the Intramural Research Program (DIRP) of the National Institute of Mental Health (NIMH), USA, ZIAMH002797, ZIAMH002971, and the BRAIN initiative Grant U19 NS107464-01. This research utilized the supercomputing resources of the National Institutes of Health (NIH, USA; Biowulf, http://hpc.nih.gov).

Author Contributions

TLR and DP conceived and planned the study; TLR, BG, and VS performed experiments; AV took the lead in holographic setup design. TLR took the lead in data analysis with support from BG and VS. SP and RS took the lead on machine learning based decoding of experimental data. All authors contributed to the analyses. TLR and DP wrote the manuscript.

Competing interests

The authors declare no competing interests.

606 ## Supplementary Figures

607 **Supplementary Figure 1**

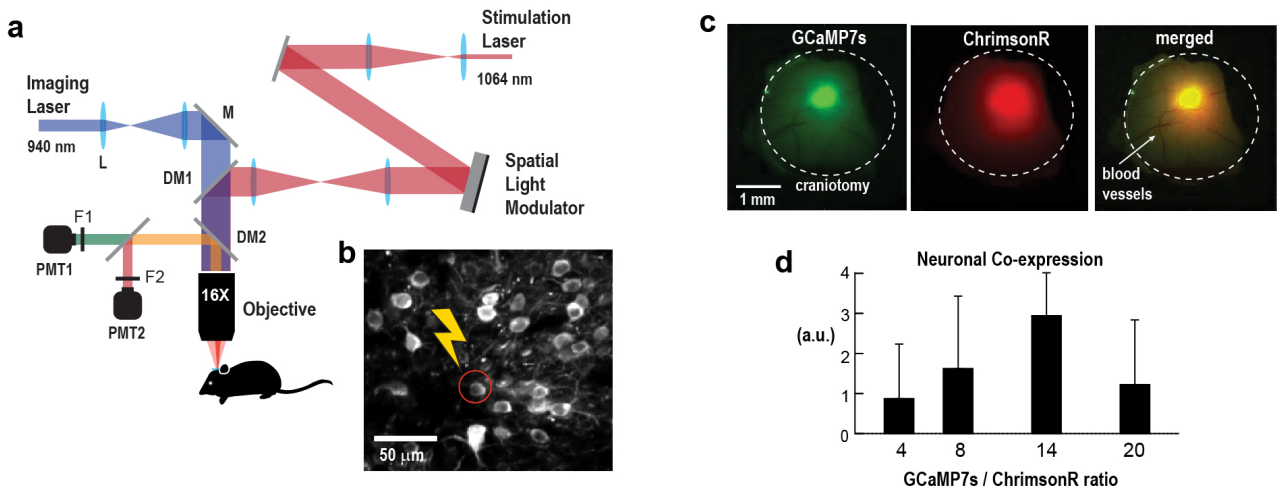

Supplementary Fig. 1 | All optical interrogation set-up to image and perturb select neuronal populations with cellular specificity. **a** Schematics of all-optical holographic stimulation combined with 2-photon imaging path (DM: dichroic mirror, M: Mirror, F: filter, PMT: photomultiplier, L: lens). **b** Mean 2-photon image in L2/3 of V1 with neurons co-expressing jGCaMP7s and ChrimsonR allowing for holographic stimulation of a single pyramidal neurons while reconstructing spike activity in the surround network using 2-PI. **c** Widefield expression image of GCaMP7s and CrimsonR across the craniotomy and corresponding merged yellow combined picture indicating co-expression (*single mouse*). **d** Co-expression of GCaMP7s with ChrimsonR pyramidal neurons over changing the titer ratio of the two corresponding virus. N = 23 mice.

608

609

610

611 **Supplementary Figure 2**

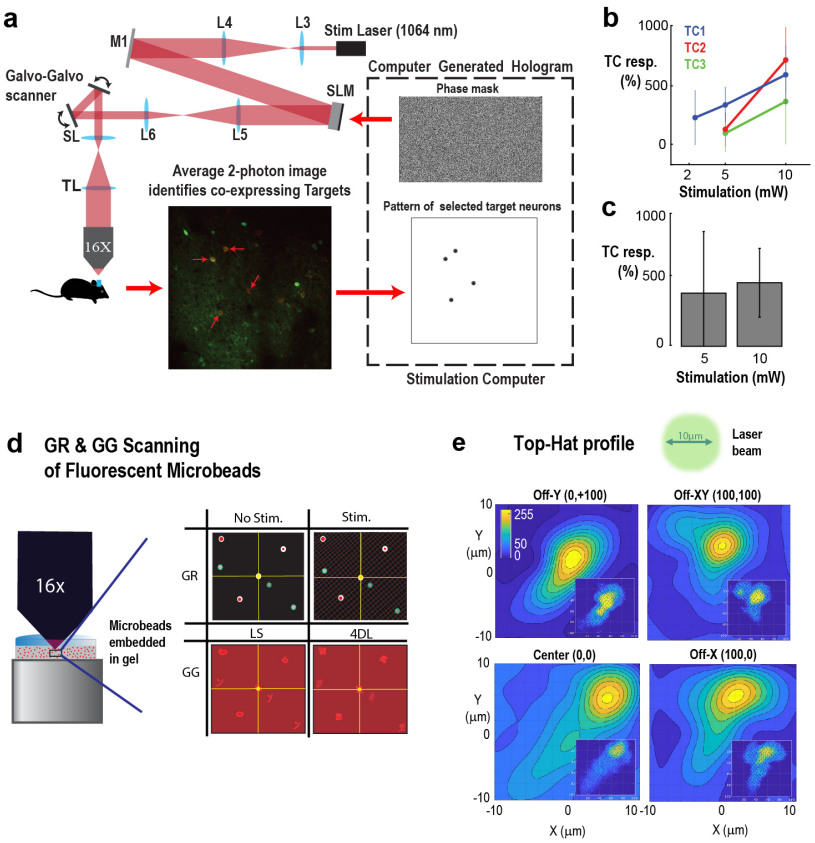

Supplementary Fig. 2 | Schematic design and evaluation of the stimulation path using spatial light modulation. a Light from the laser (Light Conversion, λ = 1064 nm, repetition rate = 600 kHz, pulse width <100 fs) is expanded (4x) to fill the area of the spatial light modulator (SLM; Meadowlark, LCoS high resolution 1920×1152 phase modulator). The hologram on the pupil plane is shrunk to fit the size of the Galvo-Galvo scanners (~3 mm diameter) that guide the stimulation beam in the focal plane of image (Nikon 16X, working distance = 3 mm and effective focal length = 12.5 mm). Neurons are manually selected from the mean 2-PI image of the field of view in both red and green channels. Target cells (TC) that express both the opsin (ChrimsonR, with tdTomato tag) and GCaMP7s are selected for stimulation and simultaneous estimation of the evoked spike count. Based on the selected targets, a map of top-hat patterns with diameter of 10 µm were used to generate the hologram on the SLM. Optical power per TC was adjusted to 5 — 10 mW, depending on the depth and expression level. **b** Spiking above base line increases with stimulation power (N = 3 TC; 100 ms stimulation duration). **c** No difference was found in evoked spike count above baseline for 5 and 10 mW stimulation when averaging across all TC. **d** Schematics of reconstruction of the stimulation xy-profile using fluorescence microbeads. Galvo-Galvo (GG) controlled stimulation of gel-embedded microbeads (3 µm diameter) and simultaneous Galvo-Resonance (GR) 2-PI of elicited response. *Circles*: Individual microbeads before and during stimulation. **e** Experimentally reconstructed and smoothed xy-profile of a flat-hat stimulation (10 µm diameter; 5 mW) at 4 different positions within the field of view at center (0,0), off-x (+100 µm, 0), off-y (0, +100 µm), and off-xy (+100 µm, +100 µm). *Inset*: Non-smoothed reconstruction.

612

613 **Supplementary Figure 3**

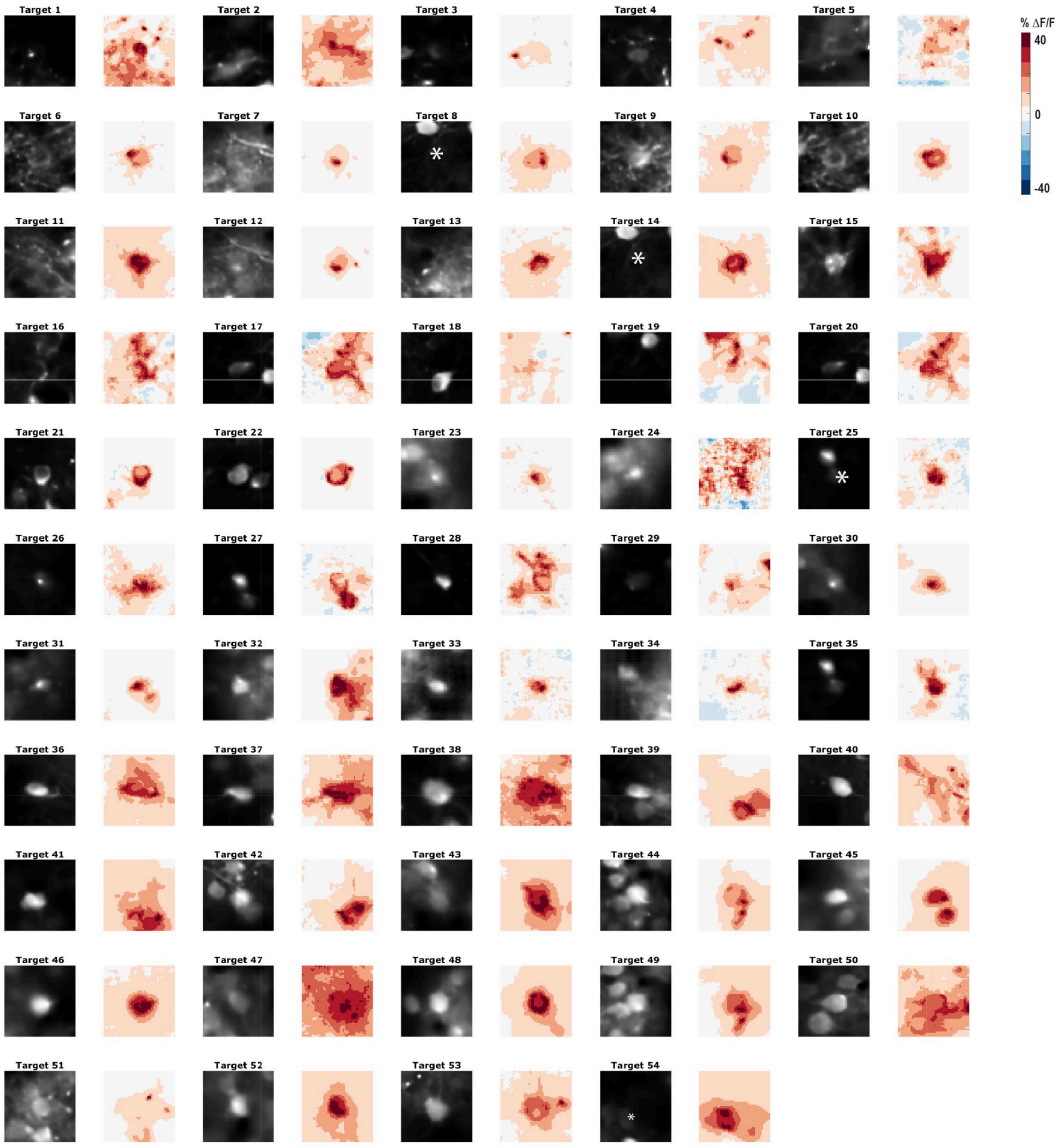

Supplementary Fig. 3 | Summary in successfully isolating individual pyramidal neurons in layer 2/3 of primary visual cortex during rest using holographic stimulation combined with 2-PI. For each TC included in the analysis the mean luminance after motion correction and denoising (*left*) and the ΔF/F in response to stimulation for each pixel in a 50×50-pixel area centered on the TC (*right*) are shown.

614
615

616 **Supplementary Figure 4**

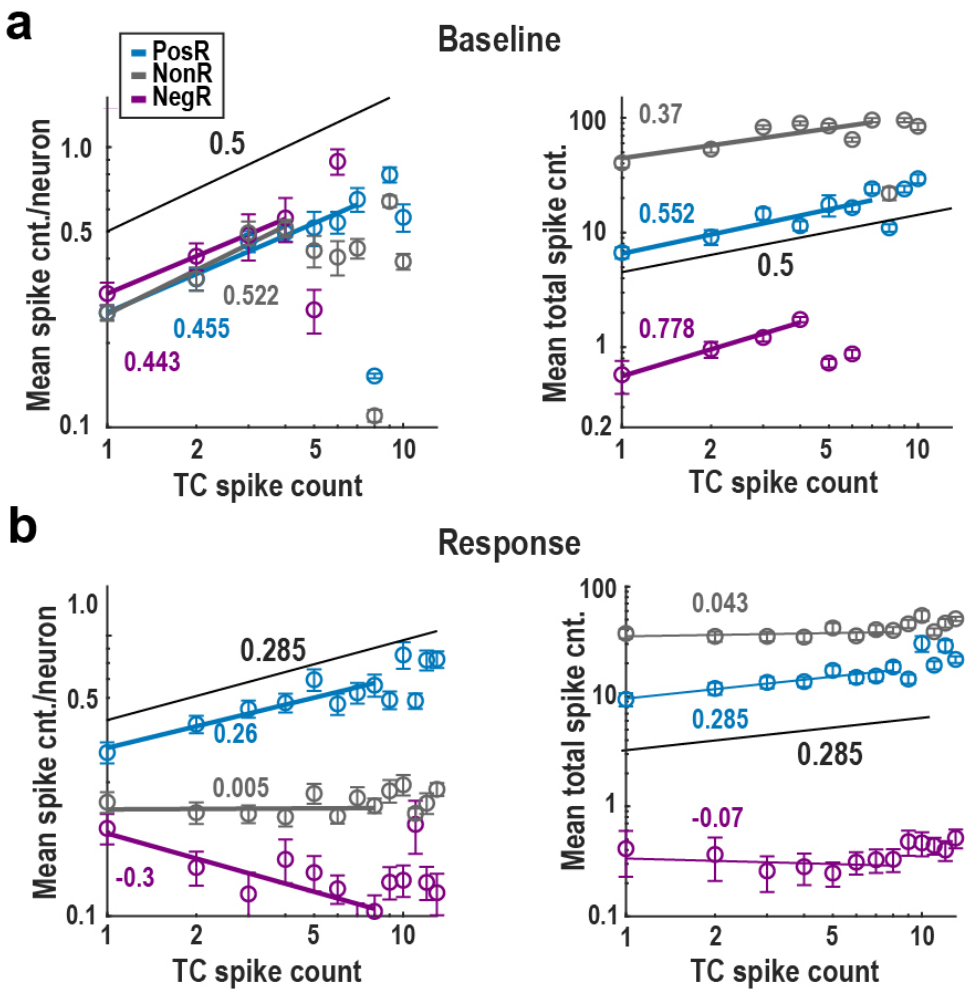

Supplementary Fig. 4 | Spike count in all different subpopulations scale with spike count of target cells during baseline activity, but only Positive Responders scale during stimulation. a Mean spike count on PosR (*blue*), NonR (*grey*) and NegR (*purple*) as function of spike count of TC, in log-log, during baseline. Power law fits are indicated by solid lines, with obtained exponents shown. *Left*: mean calculated per neuron. *Right*: mean calculated after summing over the population. **b** Same as in a, but during holographic stimulation.

617

618

619 **Supplementary Figure 5**

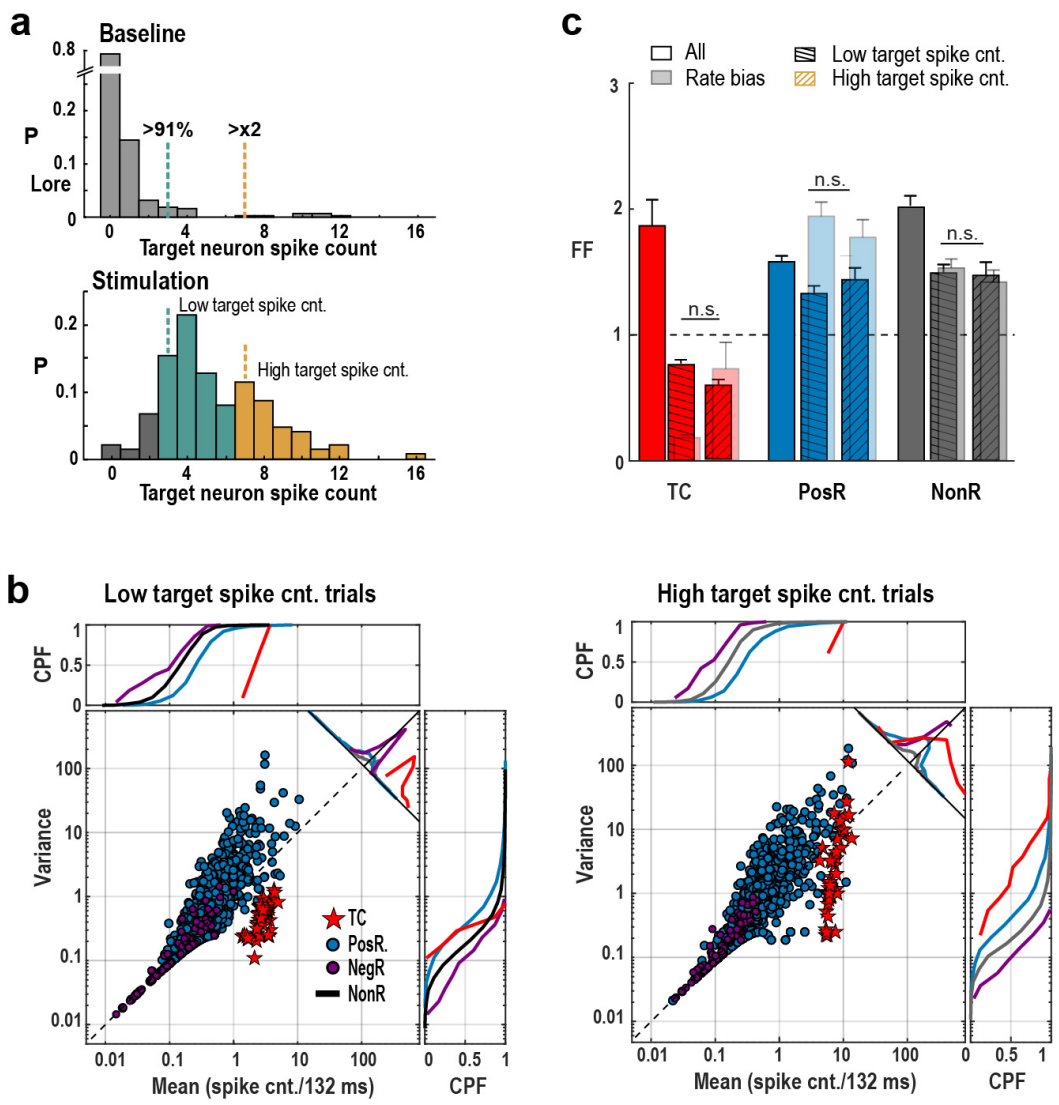

Supplementary Fig. 5 | High response variability in PosR and NonR does not originate from variability in evoked spikes of TC. a Example of separating trials from one TC into those with a high spike count and low spike count. *Top*: Spike count distribution during baseline allows for the identification of 91% threshold above chance as well as twice that threshold. *Bottom*: Using the two thresholds from the baseline distributions categorizes stimulation trials of the TC into low and high target counts, respectively. **b** Summary statistics of mean TC trials separated by low and high target counts. Note the remaining high variance of PosR despite the large drop in TC variance. **c** FF does not change if trials within a TC are separated into high and low spike counts which changes the FF for TC.

620

621 **Supplementary Figure 6**

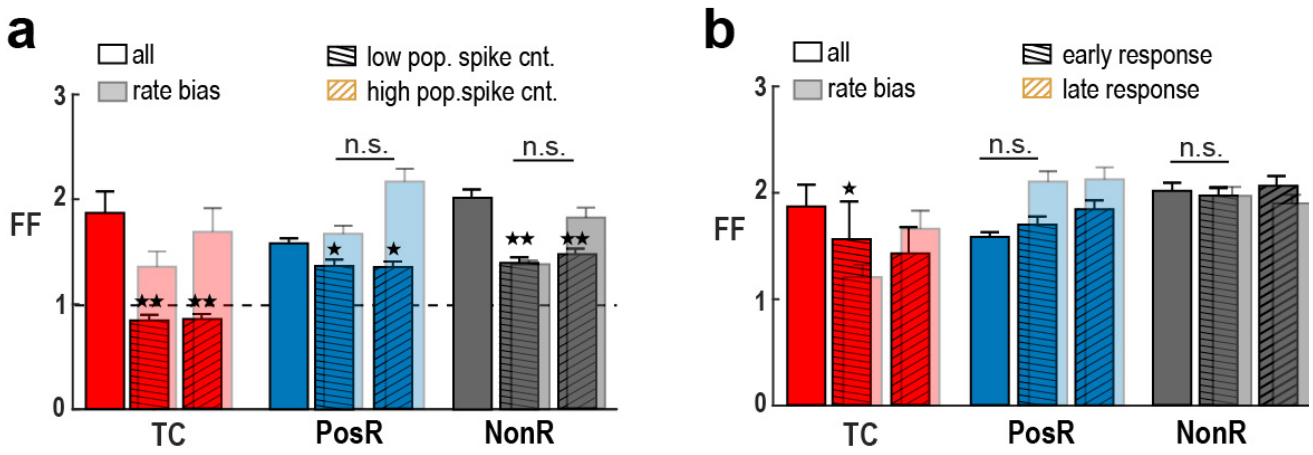

Supplementary Fig. 6 | Maintained variability during response is not due to change in preceding baseline activity and is robust throughout the response. No change in FF when subdividing into TC trials with high or low population spike count (**a**) or early vs. late spiking responses (**b**).

622

623 **Supplementary Figure 7**

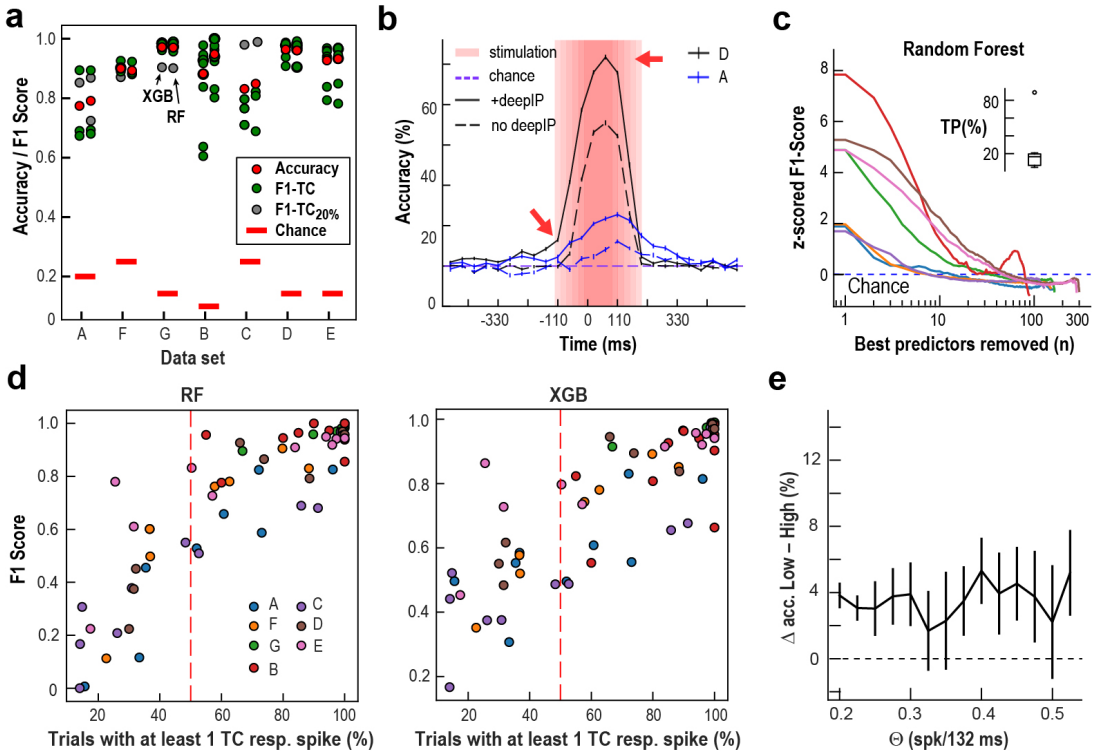

Supplementary Fig. 7 | Decoding accuracy, stimulation efficacy, impact of deep interpolation. **a** Multi-target cell stimulation experiments analyzed and corresponding break-down of TC performances. Overview of F1-scores for TCs (*green*) and TC that did not reach 20% of spike success (*gray*) upon stimulation. F1-scores are compared to chance level (*red bars*) and overall accuracy (*red*). vs. late spiking responses. XGBoost (*left*) and Random Forest (*right*) results are very similar across all datasets. **b** Deep interpolation slightly advances stimulus information and significantly increases accuracy thereby slightly prolonging transient response time. Exemplary impact for weak (A) and strong (D) data set of similar chance level (10 TC each). The enhanced accuracy achieved with Deep Interpolation demonstrates the method's noise-reducing benefits, which improve the model's ability to capture relevant neural signals. However, it also shows that it undermines our ability to study temporal progression of activations, as its window of smoothing ranges across 30 frames. **c** Z-scored F1-scores calculated for each TC and then averaged, for each dataset (same color code as in Fig. 3), as function of number of best predictors dropped. *Inset*: Average number of best predictors dropped before F1-scores reach chance levels. Random Forest method. **d** For each data set, stimulation success (at least 1 spike) varied among TC. Target stimulation success positively correlated with decoding power, i.e. F1-score, of a TC in RF and XGB. **e** Difference in accuracy for Low and High trials is small (with Low trials having slightly higher accuracy), regardless of the threshold used to separate them (cp. Fig. 4h).

624

References

1 Allen, W. E. *et al.* Global Representations of Goal-Directed Behavior in Distinct Cell Types of Mouse Neocortex. *Neuron* **94**, 891-907.e896 (2017). https://doi.org:10.1016/j.neuron.2017.04.017

2 London, M., Roth, A., Beeren, L., Häusser, M. & Latham, P. E. Sensitivity to perturbations in vivo implies high noise and suggests rate coding in cortex. *Nature* **466**, 123-127 (2010).

3 Meyer, J. F., Golshani, P. & Smirnakis, S. M. The Effect of Single Pyramidal Neuron Firing Within Layer 2/3 and Layer 4 in Mouse V1. *Frontiers in Neural Circuits* **12** (2018). https://doi.org:10.3389/fncir.2018.00029

4 Chettih, S. N. & Harvey, C. D. Single-neuron perturbations reveal feature-specific competition in V1. *Nature* **567**, 334-340 (2019). https://doi.org:10.1038/s41586-019-0997-6

5 Jouhanneau, J.-S., Kremkow, J. & Poulet, J. F. A. Single synaptic inputs drive high-precision action potentials in parvalbumin expressing GABA-ergic cortical neurons in vivo. *Nature communications* **9**, 1540 (2018). https://doi.org:10.1038/s41467-018-03995-2

6 Hemberger, M., Shein-Idelson, M., Pammer, L. & Laurent, G. Reliable sequential activation of neural assemblies by single pyramidal cells in a three-layered cortex. *Neuron* **104**, 353-369. e355 (2019).

7 O'Rawe, J. F. *et al.* Excitation creates a distributed pattern of cortical suppression due to varied recurrent input. *Neuron* **111**, 4086-4101.e4085 (2023). https://doi.org:10.1016/j.neuron.2023.09.010

8 Marshel, J. H. *et al.* Cortical layer–specific critical dynamics triggering perception. *Science*, eaaw5202 (2019). https://doi.org:10.1126/science.aaw5202

9 Carrillo-Reid, L., Han, S., Yang, W., Akrouh, A. & Yuste, R. Controlling Visually Guided Behavior by Holographic Recalling of Cortical Ensembles. *Cell* **178**, 447-457.e445 (2019). https://doi.org:10.1016/j.cell.2019.05.045

10 Houweling, A. R. & Brecht, M. Behavioural report of single neuron stimulation in somatosensory cortex. *Nature* **451**, 65-68 (2008). https://doi.org:10.1038/nature06447

11 Wolfe, J., Houweling, A. R. & Brecht, M. Sparse and powerful cortical spikes. *Curr. Opin. Neurobiol.* **20**, 306-312 (2010). https://doi.org:https://doi.org/10.1016/j.conb.2010.03.006

12 Cheng-yu, T. L., Poo, M.-m. & Dan, Y. Burst spiking of a single cortical neuron modifies global brain state. *Science* **324**, 643-646 (2009).

13 Zucca, S. *et al.* An inhibitory gate for state transition in cortex. *Elife* **6**, e26177 (2017).

14 Histed, M. H., Ni, A. M. & Maunsell, J. H. Insights into cortical mechanisms of behavior from microstimulation experiments. *Prog. Neurobiol.* **103**, 115-130 (2013). https://doi.org:10.1016/j.pneurobio.2012.01.006

15 Vaadia, E. *et al.* Dynamics of neuronal interactions in monkey cortex in relation to behavioural events. *Nature* **373**, 515-518 (1995).

16 Stringer, C. *et al.* Spontaneous behaviors drive multidimensional, brainwide activity. *Science* **364**, eaav7893 (2019). https://doi.org:doi:10.1126/science.aav7893

17 Kuhn, A., Aertsen, A. & Rotter, S. Neuronal integration of synaptic input in the fluctuation-driven regime. *J. Neurosci.* **24**, 2345-2356 (2004). https://doi.org:10.1523/JNEUROSCI.3349-03.2004

18 Arieli, A., Sterkin, A., Grinvald, A. & Aertsen, A. Dynamics of ongoing activity: Explanation of the large variability in evoked cortical responses. *Science* **273**, 1868-1871 (1996).

19 Braitenberg, V. & Schüz, A. *Anatomy of the Cortex: Statistics and Geometry*. (Springer-Verlag, 1991).

20 Thomson, A. M., West, D. C., Wang, Y. & Bannister, A. P. Synaptic connections and small circuits involving excitatory and inhibitory neurons in layers 2-5 of adult rat and cat neocortex: triple intracellular recordings and biocytin labelling in vitro. *Cereb. Cortex* **12**, 936-953 (2002).

21 Levy, R. B. & Reyes, A. D. Spatial Profile of Excitatory and Inhibitory Synaptic Connectivity in Mouse Primary Auditory Cortex. *J. Neurosci.* **32**, 5609 (2012). https://doi.org:10.1523/JNEUROSCI.5158-11.2012

22 Jouhanneau, J.-S., Kremkow, J., Dorrn, A. L. & Poulet, J. F. In vivo monosynaptic excitatory transmission between layer 2 cortical pyramidal neurons. *Cell reports* **13**, 2098-2106 (2015).

23 Campagnola, L. *et al.* Local connectivity and synaptic dynamics in mouse and human neocortex. *Science* **375**, eabj5861 (2022). https://doi.org:doi:10.1126/science.abj5861

24 Kumar, A., Rotter, S. & Aertsen, A. Spiking activity propagation in neuronal networks: reconciling different perspectives on neural coding. *Nat. Rev. Neurosci.* **11**, 615-627 (2010). https://doi.org:10.1038/nrn2886

25 Haider, B., Hausser, M. & Carandini, M. Inhibition dominates sensory responses in the awake cortex. *Nature* **493**, 97-100 (2013). https://doi.org:http://www.nature.com/nature/journal/v493/n7430/abs/nature11665.html#supplementary-information

26 Tremblay, R., Lee, S. & Rudy, B. GABAergic interneurons in the neocortex: From cellular properties to circuits. *Neuron* **91**, 260-292 (2016). https://doi.org:10.1016/j.neuron.2016.06.033

27 Chialvo, D. R., Cannas, S. A., Grigera, T. S., Martin, D. A. & Plenz, D. Controlling a complex system near its critical point via temporal correlations. *Scientific Reports* **10**, 12145 (2020). https://doi.org:10.1038/s41598-020-69154-0

28 Muñoz, M. A., Dickman, R., Vespignani, A. & Zapperi, S. Avalanche and spreading exponents in systems with absorbing states. *Phys. Rev. E* **59**, 6175-6179 (1999).

29 Capek, E. *et al.* Parabolic avalanche scaling in the synchronization of cortical cell assemblies. *Nature communications* **14**, 2555 (2023). https://doi.org:10.1101/2022.11.02.514938

30 Plenz, D. *et al.* Self-Organized Criticality in the Brain. *FrPhy* **9** (2021). https://doi.org:10.3389/fphy.2021.639389

31 Beggs, J. M. & Plenz, D. Neuronal avalanches in neocortical circuits. *J. Neurosci.* **23**, 11167-11177 (2003). https://doi.org:10.1523/JNEUROSCI.23-35-11167.2003

32 Softky, W. R. & Koch, C. The highly irregular firing of cortical cells is inconsistent with temporal integration of random EPSPs. *J. Neurosci.* **13**, 334-350 (1993).

33 Holmgren, C., Harkany, T., Svennenfors, B. & Zilberter, Y. Pyramidal cell communication within local networks in layer 2/3 of rat neocortex. *The Journal of physiology* **551**, 139-153 (2003).

34 Churchland, M. M. *et al.* Stimulus onset quenches neural variability: a widespread cortical phenomenon. *Nat. Neurosci.* **13**, 369-378 (2010).

35 Rajdl, K., Lansky, P. & Kostal, L. Fano factor: a potentially useful information. *Frontiers in computational neuroscience* **14**, 569049 (2020).

36 Marro, J. & Dickman, R. Nonequilibrium phase transitions in lattice models. *Nonequilibrium Phase Transitions in Lattice Models* (2005).

37 Chen, T. & Guestrin, C. in *Proceedings of the 22nd ACM SIGKDD International Conference on Knowledge Discovery and Data Mining* 785–794 (Association for Computing Machinery, San Francisco, California, USA, 2016).

38 Ho, T. K. in *Proceedings of 3rd international conference on document analysis and recognition.* 278-282 (IEEE).

39 Breiman, L. Random forests. *MLear* **45**, 5-32 (2001).

40 Lecoq, J. *et al.* Removing independent noise in systems neuroscience data using DeepInterpolation. *Nat. Methods* (2021). https://doi.org:10.1038/s41592-021-01285-2

41 Srinivasan, K., Ribeiro, T. L., Kells, P. & Plenz, D. The recovery of parabolic avalanches in spatially subsampled neuronal networks at criticality. *Scientific Reports* **14**, 19329 (2024). https://doi.org:10.1038/s41598-024-70014-4

42 Yu, S., Klaus, A., Yang, H. & Plenz, D. Scale-invariant neuronal avalanche dynamics and the cut-off in size distributions. *PLoS One* **9**, e99761 (2014). https://doi.org:10.1371/journal.pone.0099761

43 Seeman, S. C. *et al.* Sparse recurrent excitatory connectivity in the microcircuit of the adult mouse and human cortex. *eLife* **7**, e37349 (2018). https://doi.org:10.7554/eLife.37349

44 Abeles, M. *Corticonics: Neural Circuits of the Cerebral Cortex*. Vol. 1 (Cambridge University Press, 1991).

45 Diesmann, M., Gewaltig, M. O. & Aertsen, A. Stable propagation of synchronous spiking in cortical neural networks. *Nature* **402**, 529-533 (1999). https://doi.org:10.1038/990101

46 Prechtl, J. C., Cohen, L. B., Pesaran, B., Mitra, P. P. & Kleinfeld, D. Visual stimuli induce waves of electrical activity in turtle cortex. *Proc.Natl.Acad.Sci.U.S.A* **94**, 7621-7626 (1997).

47 Rubino, D., Robbins, K. A. & Hatsopoulos, N. G. Propagating waves mediate information transfer in the motor cortex. *Nat. Neurosci.* **9**, 1549-1557 (2006).

48 Singer, W. Cortical dynamics revisited. *Trends Cogn Sci* (2013).

49 Gray, C. M., Konig, P., Engel, A. K. & Singer, W. Oscillatory responses in cat visual cortex exhibit inter-columnar synchronization which reflects global stimulus properties. *Nature* **338**, 334-337 (1989).

50 Lisman, J. E. Bursts as a unit of neural information: making unreliable synapses reliable. *Trends Neurosci.* **20**, 38-43 (1997).

51 Riquelme, J. L., Hemberger, M., Laurent, G. & Gjorgjieva, J. Single spikes drive sequential propagation and routing of activity in a cortical network. *eLife* **12**, e79928 (2023). https://doi.org:10.7554/eLife.79928

52 Shu, Y., Hasenstaub, A., Badoual, M., Bal, T. & McCormick, D. A. Barrages of synaptic activity control the gain and sensitivity of cortical neurons. *J. Neurosci.* **23**, 10388-10401 (2003).

53 Tsodyks, M., Uziel, A. & Markram, H. Synchrony generation in recurrent networks with frequency-dependent synapses. *J. Neurosci.* **20**, RC50 (2000).

54 Molnár, G. *et al.* Complex Events Initiated by Individual Spikes in the Human Cerebral Cortex. *PLoS Biol.* **6**, e222 (2008). https://doi.org:10.1371/journal.pbio.0060222

55 Ferrarese, L. *et al.* Dendrite-Specific Amplification of Weak Synaptic Input during Network Activity In Vivo. *Cell Reports* **24**, 3455-3465.e3455 (2018). https://doi.org:https://doi.org/10.1016/j.celrep.2018.08.088

56 Harris, K. D. & Mrsic-Flogel, T. D. Cortical connectivity and sensory coding. *Nature* **503**, 51-58 (2013). https://doi.org:10.1038/nature12654

57 Histed, M. H. & Maunsell, J. H. Cortical neural populations can guide behavior by integrating inputs linearly, independent of synchrony. *Proc. Natl. Acad. Sci. U. S. A.* **111**, E178-187 (2014). https://doi.org:10.1073/pnas.1318750111

58 Barth, A. L. & Poulet, J. F. A. Experimental evidence for sparse firing in the neocortex. *Trends Neurosci.* **35**, 345-355 (2012).

59 Kinouchi, O. & Copelli, M. Optimal dynamical range of excitable networks at criticality. *Nat. Phys.* **2** 348-351 (2006).

60 Stevens, S. S. *Psychophysics: Introduction to its perceptual, neural and social prospects*. (Routledge, 2017).
61 Assis, V. R. & Copelli, M. Dynamic range of hypercubic stochastic excitable media. *Phys Rev E Stat Nonlin Soft Matter Phys* **77**, 011923 (2008). https://doi.org:10.1103/PhysRevE.77.011923
62 Jun, N. Y. *et al.* Coordinated multiplexing of information about separate objects in visual cortex. *eLife* **11**, e76452 (2022). https://doi.org:10.7554/eLife.76452
63 Caruso, V. C. *et al.* Single neurons may encode simultaneous stimuli by switching between activity patterns. *Nature communications* **9**, 2715 (2018). https://doi.org:10.1038/s41467-018-05121-8
64 Levy, M., Sporns, O. & MacLean, J. N. Network analysis of murine cortical dynamics implicates untuned neurons in visual stimulus coding. *Cell Reports* **31** (2020). https://doi.org:10.1016/j.celrep.2020.03.047
65 Scott, G. *et al.* Voltage imaging of waking mouse cortex reveals emergence of critical neuronal dynamics. *J. Neurosci.* **34**, 16611 - 16620 (2014). https://doi.org:10.1523/JNEUROSCI.3474-14.2014
66 Bellay, T., Klaus, A., Seshadri, S. & Plenz, D. Irregular spiking of pyramidal neurons organizes as scale-invariant neuronal avalanches in the awake state. *eLife* **4**, e07224 (2015). https://doi.org:10.7554/eLife.07224
67 Bellay, T., Shew, W. L., Yu, S., Falco-Walter, J. J. & Plenz, D. Selective participation of single cortical neurons in neuronal avalanches. *Frontiers in Neural Circuits* **14** (2021). https://doi.org:10.3389/fncir.2020.620052
68 Capek, E. *et al.* Parabolic avalanche scaling in the synchronization of cortical cell assemblies. *Nature communications* **14**, 2555 (2023).
69 Petermann, T. *et al.* Spontaneous cortical activity in awake monkeys composed of neuronal avalanches. *Proc. Natl. Acad. Sci. U.S.A.* **106**, 15921-15926 (2009). https://doi.org:10.1073/pnas.0904089106
70 Beggs, J. M. & Plenz, D. Neuronal avalanches are diverse and precise activity patterns that are stable for many hours in cortical slice cultures. *J. Neurosci.* **24**, 5216-5229 (2004).
71 Stewart, C. V. & Plenz, D. Inverted-U profile of dopamine-NMDA-mediated spontaneous avalanche recurrence in superficial layers of rat prefrontal cortex. *J. Neurosci.* **26**, 8148-8159 (2006). https://doi.org:10.1523/JNEUROSCI.0723-06.2006
72 Lombardi, F., Herrmann, H. J., Plenz, D. & de Arcangelis, L. Temporal correlations in neuronal avalanche occurrence. *Scientific Reports* **6**, 24690 (2016). https://doi.org:10.1038/srep24690
73 Lombardi, F., Herrmann, H., Plenz, D. & de Arcangelis, L. On the temporal organization of neuronal avalanches. *Front. Syst. Neurosci.* **8**, 204 (2014). https://doi.org:10.3389/fnsys.2014.00204
74 Goldey, G. J. *et al.* Removable cranial windows for long-term imaging in awake mice. *Nature Protocols* **9**, 2515 (2014). https://doi.org:10.1038/nprot.2014.165
75 Dana, H. *et al.* High-performance GFP-based calcium indicators for imaging activity in neuronal populations and microcompartments. *bioRxiv* (2018).
76 Klapoetke, N. C. *et al.* Independent optical excitation of distinct neural populations. *Nat. Methods* **11**, 338 (2014). https://doi.org:10.1038/nmeth.2836
https://www.nature.com/articles/nmeth.2836#supplementary-information
77 Juavinett, A. L., Nauhaus, I., Garrett, M. E., Zhuang, J. & Callaway, E. M. Automated identification of mouse visual areas with intrinsic signal imaging. *Nature Protocols* **12**, 32-43 (2017). https://doi.org:10.1038/nprot.2016.158

78 Sit, K. K. & Goard, M. J. Distributed and retinotopically asymmetric processing of coherent motion in mouse visual cortex. *Nature communications* **11**, 1-14 (2020).
79 Kleiner, M., Brainard, D. & Pelli, D. What's new in Psychtoolbox-3? (2007).
80 Adesnik, H. & Abdeladim, L. Probing neural codes with two-photon holographic optogenetics. *Nat. Neurosci.* **24**, 1356-1366 (2021). https://doi.org:10.1038/s41593-021-00902-9
81 Pachitariu, M. *et al.* Suite2p: beyond 10,000 neurons with standard two-photon microscopy. *bioRxiv*, 061507 (2017). https://doi.org:10.1101/061507
82 Pedregosa, F. Scikit-learn: Machine learning in python Fabian. *Journal of machine learning research* **12**, 2825 (2011).
83 Shapley, L. S. Notes on the n-person game—ii: The value of an n-person game. (RAND Coorperation, Santa Monica, CA, USA, 1951).
84 Scott, M. & Su-In, L. A unified approach to interpreting model predictions. *Advances in neural information processing systems* **30**, 4765-4774 (2017).
85 Poil, S. S., Hardstone, R., Mansvelder, H. D. & Linkenkaer-Hansen, K. Critical-state dynamics of avalanches and oscillations jointly emerge from balanced excitation/inhibition in neuronal networks. *J. Neurosci.* **32**, 9817-9823 (2012).
86 Villegas, P., Di Santo, S., Burioni, R. & Muñoz, M. A. Time-series thresholding and the definition of avalanche size. *Phys. Rev. E* **100** (2019). https://doi.org:10.1103/PhysRevE.100.012133
87 Capek, E. *et al.* (Zenodo, 2023).